AUT Journal of Mechanical Engineering

AUT J. Mech. Eng., 7(4) (2023) 389-418
DOI: 10.22060/ajme.2024.23011.6092

Exploring Flame Characteristics of CH4/CO2/Ammonia/Air Mixtures under Elevated Conditions: An Interferometry-Based Investigation

Mehrdad Kiani[1], Ali Akbar Abbasian Arani[1]*, Mehdi Ashjaee[2], Ehsan Houshfar[2]

[1] Faculty of Mechanical Engineering, University of Kashan, Kashan, Iran
[2] School of Mechanical Engineering, College of Engineering, University of Tehran, Tehran, Iran

ABSTRACT: Ammonia (NH3) stands out as a leading option for large-scale renewable energy storage and long-distance transportation. By incorporating landfill gas and raising initial reactant temperatures, NH3 reactivity is effectively enhanced in gas turbines and boilers. This study focuses on exploring the laminar flame propagation of NH3/landfill mixtures under elevated conditions. Accurate predictions for laminar burning velocity were achieved through numerical simulations employing Ansys Chemkin-Pro, along with the San Diego, Okafor, and GRI-Mech 3.0 mechanisms. Elevating pressure from 1 to 10 bar resulted in a reduction in laminar burning velocity from 16.1 to 6 cm/s, ultimately leading to an increase in adiabatic flame temperature from 2102 to 2143 attributable to changes in combustion equilibrium. Also, the results underscored the significant influence of ammonia concentration on augmenting laminar burning velocities. In cases with higher laminar burning velocity, the proportion of NH3 added tends towards zero, while in cases with lower laminar burning velocity, the addition ratio of NH3 tends towards one. The addition of ammonia leads to a reduction in the pool of radicals. Put simply, because ammonia has a lower laminar burning velocity, the overall Laminar burning velocity of the mixture is reduced as the concentration of ammonia in the fuel mixture increases.

Review History:

Received: Feb. 23, 2024
Revised: May, 19, 2024
Accepted: Jun. 16, 2024
Available Online: Jul. 11, 2024

Keywords:

Laminar Burning Velocity
Landfill Gas (LFG)
Kinetic Model
Elevated Conditions
Ammonia Concentration

1- Introduction

There has been intense interest in using ammonia (NH_3) in combustion systems as a carbon-free fuel for gas turbines, considering its outstanding potential and developed infrastructures for production, storage, and transportation [1-3]. It should also be noted that employing NH_3 in combustion systems has also been challenged because of the narrow range of flammability, dull flame propagation, and low intensity of combustion that is attributed to it. It has been shown before that [4-6], NH_3/Air Mixtures Exhibit Slower Peak Laminar Burning Velocities (6.4-8.1 cm/s) Compared to Hydrocarbon, Syngas, and hydrogen (H_2) Fuels. Consequently, research must be done on enhancing the reactivity of NH_3 combustion systems in gas turbines. Researchers have shown that fuel enhancement [6-8] and enrichment of oxygen [5] would enhance NH_3 LBVs; expressly, fuel enhancement is highly accepted when doping of more reactive fuels is carried out. [6-9].

There has been extensive research on combustion specifications of substitute fuels that are also renewable and environmentally friendly, among which biogas is preferred due to its multitudinous advantages, including copious available resources (quickly produced from biological waste and biomass depletion). However, differing based on the resource and production procedures, the composition of landfill gas (LFG) is mainly 33% to 50% methane, with the rest of it as carbon dioxide (CO_2) (10)]. The fuel mixture's unpredictable nature results in variability of combustion characteristics causing many troubles with its usage. Thus, its foundational combustion characteristics must be determined in industrial combustors (high-pressure use) such as spark-ignited and dual-fuel engines and gas turbines. LFG might be considered a promising candidate among the primary energy sources. Biogas has a smaller burning velocity, more confined flame-stability limits, lower heating value, and higher auto-ignition temperature than methane. [11, 12]. Laminar burning velocity, as a critical characteristic of any fuel, is also a fundamental property of biogas, and it depends on pressure, temperature, and, more importantly, the reactant composition, which makes it a crucial parameter in evaluating fuel reactivity to study the mechanisms of chemical reactions [13, 14]. Also, important information on diffusivity can be extracted from the laminar burning velocity. With the help of its data, the released energy in the combustion of a specific flammable mixture can be directly controlled [15]. Furthermore, as for the gas turbines, laminar premixed burning velocities are used to predict dynamic instabilities, blow-off, and flash-back; also, generally, this tool is utilized for assessing flame stability and extinguishing capacity, as well as verifying and constructing chemical kinetics models. [16].

In a combined numerical-experimental approach, Kiani, Houshfar [17] studied premixed landfill/air flames LBV,

*Corresponding author's email: abbasian@kashanu.ac.ir

flammability, and temperature distribution in different equivalence ratios in intersecting burners. The flame temperature distribution and burning velocity were measured in their work using flame visualization via the Mach-Zehnder method. CO_2 was used as the diluent with percentages varying from 0 to 50, and LBV and temperature field data of CO_2 and methane mixtures were reported at atmospheric pressures and temperatures in their experiments. Yet, not much experimental research has been carried out on Landfill gas combustion and its characteristics at high pressures (either numerical or low pressures).

Wang et al. [18] employed numerical methods to examine the flame structure of a $CH_4/CO_2/H_2O$ counter flow diffusion flame at ambient pressure and temperature. They varied the CO_2 mole fraction in the fuel mixture from 0 to 0.6. Altering the CO_2 concentration in the fuel mixture from zero to 20%, Hu, Jiang [19] numerically studied the influence of diluents ($He/Ar/N_2/CO_2$) on the methane-air mixtures' LBV. Even though there have been a significant number of studies investigating Methane and CO_2 combustion characteristics, they have been chiefly concerned with mixtures that are very different from typical compositions of landfill fuel. Oppositely, most industrial combustion apparatus perform based on premixed flame propagation at upraised pressures. Consequently, studies must be carried out on the influence of pressure on the combustion characteristics of target fuels. Yet, not much experimental research has been carried out on Landfill gas combustion and its characteristics at high pressures (either numerical or low pressures).

Many studies have been conducted on the combustion characteristics of biogas flames, but so far, no information has been provided regarding the combination of Landfill gas and ammonia gas. Since information regarding combustion characteristics such as laminar burning velocity and temperature for the mixture of Landfill/Ammonia at elevated pressure and temperature is incomplete, this study investigates the thermodynamic combustion characteristics of the mixture using an experimental interferometry approach. Besides, a kinetic model for these mixtures was used for normal to elevated conditions. Experiments were carried out at different Ammonia mole ratios ($\propto$), methane mole fraction (β), pressures (P_i) and temperatures (T_i). Setup and model validation were done using the experimental data obtained in our study and the data existing in the prior literature, including S_L of NH_3/landfill/air mixtures. To investigate the influence of fuel composition, an analysis of sensitivity and flux of consumption was carried out on the laminar flame propagation characteristics.

2- Experimental setup

2- 1- Experimental facilities and procedure

In the present work, a combustion chamber made of steel in a cylindrical shape with a length of 280 mm, an inner diameter of 225 mm, and a volume of 11 L was used for the experiments. The setup, the attached equipment, and images of flame propagation are shown in Fig. 1. Stainless steel rods were employed to fabricate the electrodes for the spark ignition system. The spark plugs are placed on the two

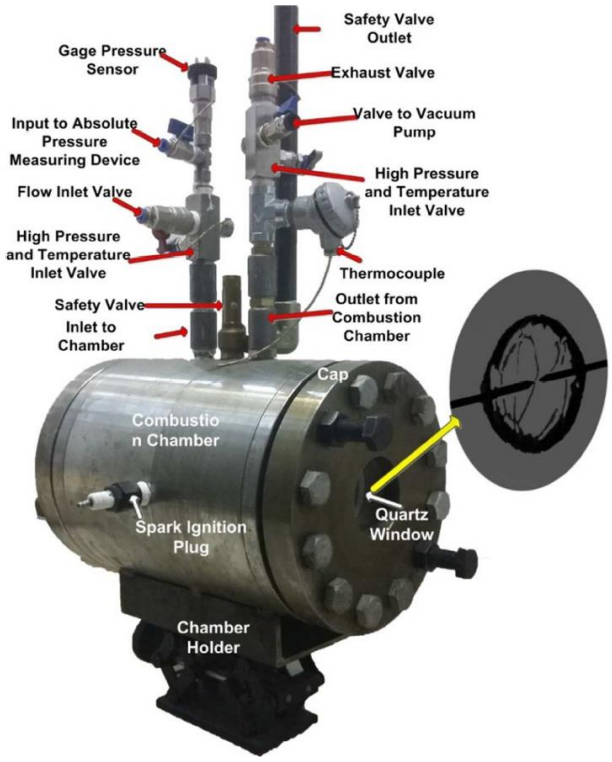

Fig. 1. The equipment connected to the combustion chamber (21)

different sides of the chamber in parallel concentric holes. A capacitive (electrode distance of 0.5 mm to 2 mm) discharge circuit was used for sparking with a 10 kV discharge voltage. The combustion ignition energy in a capacitor discharge ignition (CDI) system varied between 0.5 and 3.2 J, primarily influenced by the fuel mixture composition and temperature. As for the optical visualization, 80 mm in length and 100 mm in diameter, the chamber is fitted with two quartz windows, each mounted on a separate side. Schlieren photography was enabled via two pairs of parallel flanges that can keep the quartz opening in its place. Three slots are designed at the upper part of the chamber: one for the inlet, one for the outlet, and one serving as the safety valve (triggered when the pressure is above 50 bar). High-pressure-temperature valves are used to desperate the combustion chamber from the outlet and inlet, and two pressure sensors were located before them to monitor inside pressure. By passing a K-type thermocouple with the accuracy of ±5 K through the exhaust port into the combustion chamber, it was possible to obtain precise measurements of the initial internal temperature. Before each experiment, the chamber is evacuated using a vacuum pump by connecting it to a valve placed on the gas discharge line. The method of partial pressure was then used to fill in the intended gas compositions. After each inquiry, the chamber was refilled with air and periodically let out to remove the combustion by-products and cool the chamber's inside walls. An absolute pressure sensor (range of 0 to 1.1 bar) and a gauge pressure sensor (range of ambient pressure to 10 bar) were used to accurately measure in-cylinder pressure, which helped us precisely measure the partial pressure and indicate the mixture composition. The maximum pressure measurement error was below 0.5% of the recorded value. This claim was confirmed by measuring the transient pressure inside the chamber using a piezoelectric high-temperature dynamic pressure sensor. The maximum pressure variation for all cases was limited to 2.21%, which verifies the constant pressure flame propagation assumption. A minimum flame radius of 5 mm was also selected for flame speed measurements to diminish the ignition disturbances. To obtain a consistent flame velocity during experiments, the valves were closed and the gas was allowed to settle for approximately 20 minutes to attain a uniform mixture. This duration was determined through experimentation, ensuring that flame velocity remained unaffected even with longer resting periods. A similar mechanism to mix the gases was used, which shed more light on previous work (20)]. In this paper, experiments were repeated three to five times for each of the experimental cases to reduce the uncertainty, and average values were reported.

2- 2- Interferometry technique

2- 2- 1- The Schlieren system

The Schlieren photography system was set up with a light source of 1000 mW green diode laser ($\lambda = 520\ nm$). To create a point light source, a microscope objective with a conical length of 6 mm and a pinhole measuring 4 μm in diameter were employed to expand the light beam. A doublet (focal length = 500 mm, diameter = 100mm) is perpendicular to the laser beam for generating a parallel light beam. The 11-liter chamber is placed after the doublet. A second identical doublet was placed after the chamber to focus the light beam into a pinhole with a variable diameter. A high-speed camera (10000 fps with 960×540 resolution) was used for recording flame propagation images that were also shown on a screen for instant control (Fig. 2). The spatial resolution of the camera is roughly 0.1 mm. A cylinder containing carbon dioxide and another one containing methane was used to make various landfill compositions (volumetric fraction of methane with 50% to 100 %); gas regulators controlled these cylinders' pressure. All the gases have a purity of a minimum of 99.99%. A compressor supplied air, and a water trap was used for dehumidification. A gas splitter was used to introduce the gases to the chamber separately (Fig. 2).

2- 2- 2- Mach-Zehnder interferometry

Thermocouples and resistance thermometers are common devices for measuring temperature in different locations of the flow. Utilizing such devices is not recommended as they decrease the accuracy of measurement by disturbing the flame arrangement. The temperature of the flame can be captured by the interferometry method instantly, with no physical contact [22]. Mach-Zehnder interferometry is widely used to visualize combustion products' refraction index to attain maximum flame temperature and temperature distribution. Mach-Zehnder method's main components are microlens, two beam splitters, three mirrors, a pinhole, a camera, two doublets, a computer, and most importantly laser, which are all placed on the optical table (Fig. 3). A He-Ne source (5 mW and $\lambda = 632.8$) is used to produce the laser beams which passed through a pinhole and microlens. After passing through a compiler (10 cm in diameter), the spread beam arrives at the 50% mirror. Half of the beam is obstructed by the flame region, while the other half traverses the environment with no alteration to its refractive index. Subsequently, the split beams join. Because of the constructive and destructive phases of the two beams, dark and bright lines appear on the mirror and are recorded using a 30-fps (frame per second) digital camera and later transferred to the computer. Previous fundamental research contains more fully elaborated information on Mach-Zehnder interferometry [23, 24]. To ensure fuel humidity, a lengthy tube was employed between the mixer and slot burner, ensuring thorough homogenization before reaching the nozzle. Landfill gas production involved methane, carbon dioxide, and ammonia transfer from three capsules to mixing chambers via three rotameters. Within the mixing chamber, fuel is mixed with air injected by a compressor operating at 5 bar pressure, with flow rate measured by a Dwyer rotameter. Validation of interferometry data employed a type K thermocouple. Laboratory environment pressure and humidity were monitored through experiments, all conducted under controlled conditions at 0.87 bar pressure and 300 K temperature.

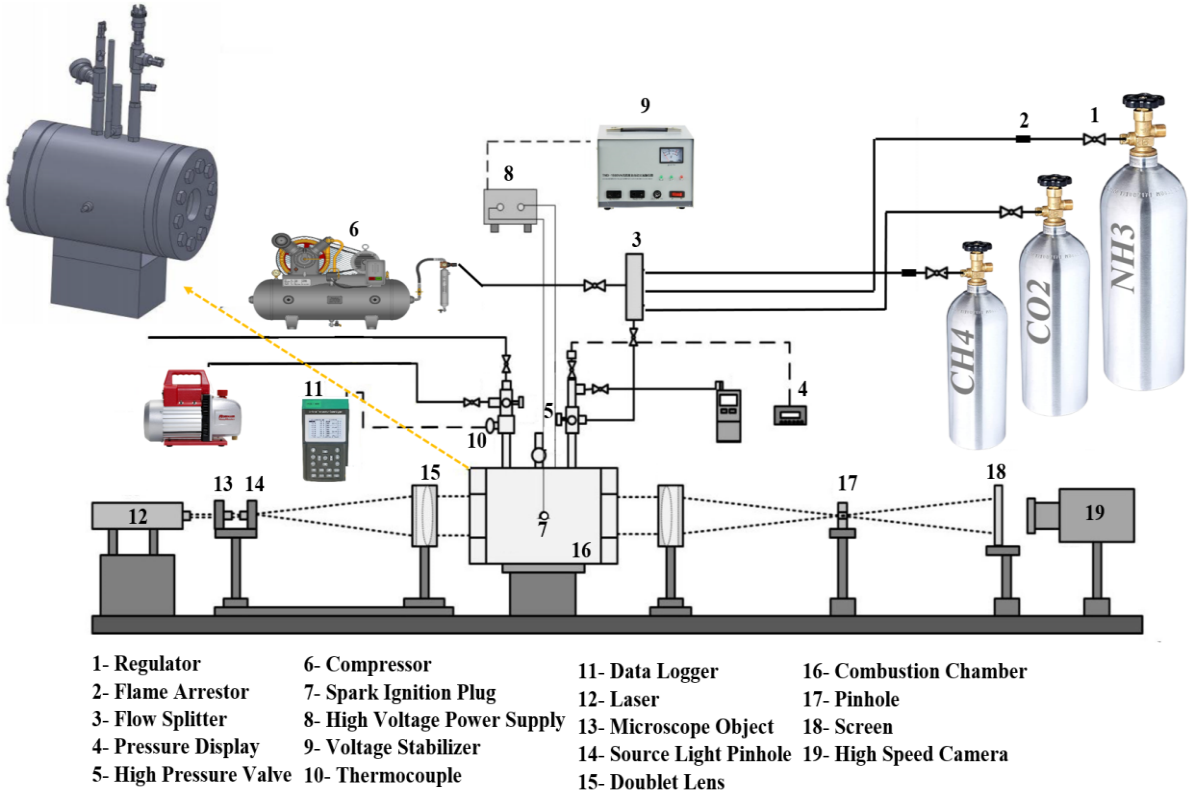

Fig. 2. Schematic of the experimental setup

3- Numerical Simulation

One-dimensional stable laminar algorithm Ansys Chemkin-Pro [25] is utilized to simulate a freely propagating adiabatic premixed flame. To resolve the steady-state conservation equations of mass, species, and energy, a hybrid technique of time integration and Newton iteration is employed by the PREMIX code. In addition to conducting experiments, an Ansys Chemkin-Pro one-dimensional simulation was performed to compute the unstretched laminar burning velocity and species concentration where its boundary conditions correspond to zero time (t=0). Temperature, pressure, and mixture composition are specified at zero time conditions. To increase the accuracy of the simulations, the multicomponent formulation was used to determine the species diffusion coefficients and fluxes [26].

The simulations were all adjusted to achieve a grid-independent solution. The computations included thermal diffusion (Soret effect) and a mixture-averaged transport formulation. Three well-known chemical kinetic mechanisms of GRI-Mech 3.0 [6], San Diego [27] (including Nitrogen chemistry), and Okafor [7] are used for detailed simulation of combustion phenomena. The GRI-Mech 3.0 contains 325 reactions and 53 species. The San Diego mechanism, on the other hand, has 311 reactions and 68 species, while the Okafor mechanism has 356 reactions and 59 species. Methodology to determine the laminar burning velocity

3- 1- Mathematical model

At the center of the chamber, the flame ignites and expands in a spherical shape. To calculate the radius of the flame front based on images of flame propagation, a circle is fitted onto it at every moment, as shown in Fig. 4. To avoid the spark rods from impacting the computation, a 30-degree area around the rods' circumference was excluded from the computed data. The information on flame radius versus time was used to derive stretched flame propagation speed (S_b) using the following equation (1):

$$S_b = \frac{dR_f}{dt} \tag{1}$$

Where R_f represents the flame front radius at any moment, which is depicted in Fig. 4. Equation (2) relates to burning speed (S_u) to stretched laminar flame speed:

$$S_u = \frac{S_b}{\sigma} \tag{2}$$

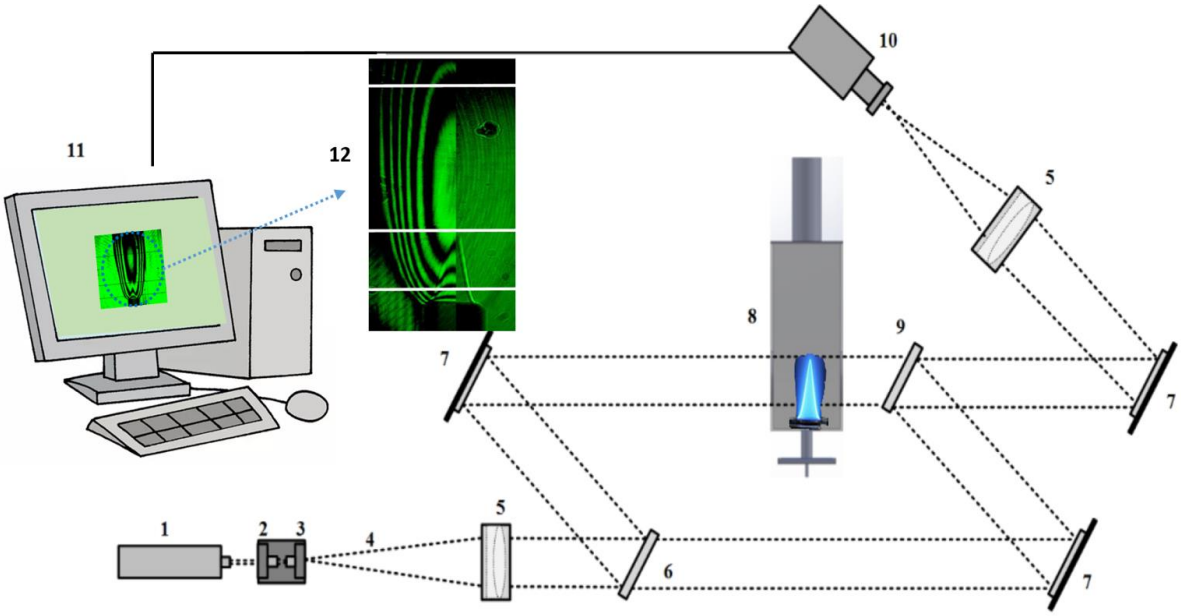

1- Laser	5- Doublet	9- Second Beam Splitter
2- Microscope	6- First Beam Splitter	10- CCD Camera
3- Pinhole	7- Mirror	11- PC
4- Laser Beam	8- Test Section	12- Output Image

Fig. 3. The experimental apparatus installed on the optical table with a schematic representation of the bright and dark lines (Mach-Zehnder).

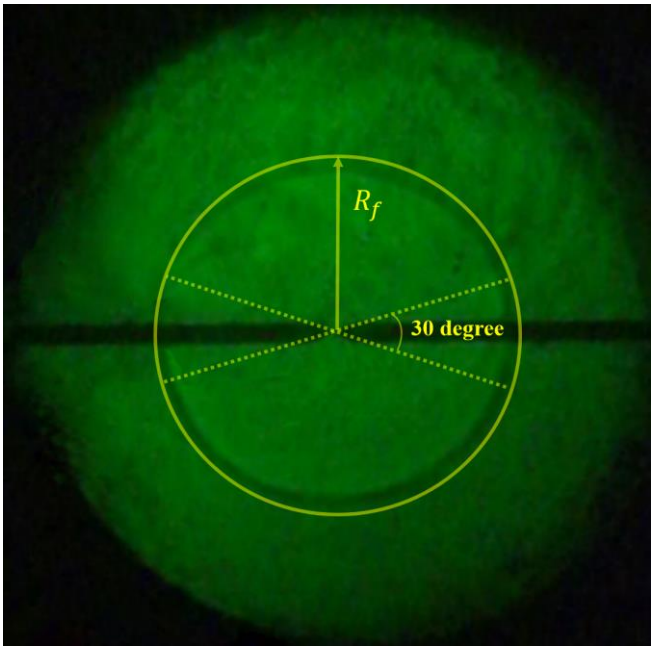

Fig. 4. The flame front visualization image

Table 1. Mesh independency test at x_{CH4} =1

	GRAD	CURV	LBV (cm/s)
1	0.12	0.2	36.5
2	0.09	0.15	35.7
3	0.06	0.1	35.3
4	0.03	0.05	35
5	0.0075	0.01	34.96
6	0.0035	0.005	34.95

In which $\sigma = \frac{\rho_u}{\rho_b}$ is the expansion ratio of the gas and ρ_b and ρ_u are densities of the burned and unburned gases, accordingly.

A spherical flame's stretch rate (κ) [28] can be expressed using the following equation (3):

$$\kappa = \frac{1}{A}\frac{dA}{dt} \tag{3}$$

In which A is the flame front's surface area, and the stretch rate can be calculated using the following equation (4) when dealing with a spherically expanding flame:

$$\kappa = \frac{1}{A}\frac{dA}{dt} = \frac{1}{R_f^2}\frac{dR_f^2}{dt} = \frac{2}{R_f}\frac{dR_f}{dt} \tag{4}$$

Once the calculations of the flame front radius are completed, to obtain the laminar flame speed values, it becomes necessary to modify the raw data to eliminate the effects of stretch rate. Therefore, after computing the flame front radius and obtaining the laminar flame speed values, the raw data is modified to eliminate the influence of stretch from the computed results. In previous studies, non-linear and linear results are offered to calculate unstretched laminar flame speed. In the latter approach, which is derived from asymptotic analysis/studies [29-31], the following equation (5) is used to correct the flame speed stretch calculated results:

$$S_b = S_b^0 - L_b.\kappa \tag{5}$$

On the other hand, in the nonlinear technique, correction is obtained by the following equation (6) [32]:

$$\left(\frac{S_b}{S_b^0}\right)^2 \ln\left(\frac{S_b}{S_b^0}\right) = -\frac{L_b\kappa}{S_b^0} \tag{6}$$

In which L_b is the Markestein length, a constant value on the order of the thickness of the flame representing the effect of flame structure on the flame speed [33] S_b represents the stretched laminar flame speed, and S_b^0 is the unstretched laminar flame speed. In the present work, the non-linear technique was used for reducing the speed of unstretched flame propagation and to get more accurate results.

3- 2- Validation and uncertainties

3- 2- 1- Validation

The accuracy and reliability of the kinetics model used in predicting the laminar burning velocities of NH3/air flames in landfill mixtures were verified. Furthermore, the simulation results obtained from three separate kinetic mechanisms were compared with relevant experimental data sourced from the literature [6, 7]. The validated kinetic mechanisms entail the GRI-Mech 3.0 (which comprises 325 reactions and 53 species), the San Diego mechanism (with 311 reactions and 68 species), and the Okafor mechanism (consisting of 356 reactions and 59 species). In Fig. 5, the simulation outcomes and experimental values were compared for diverse mole fractions of methane at pressures and temperatures of 1 atm and 298 K, respectively. Results indicate that the predictions of the laminar burning velocities made by the Okafor mechanism were in excellent agreement with experimental data, in contrast, those generated by the San Diego mechanism and GRI-Mech 3.0 were lower than the experimental values. Therefore, the Okafor mechanism is more accurate in estimating laminar burning velocities than the San Diego mechanism and GRI-Mech 3.0. Subsequent analysis and discussions will, thus, employ the Okafor mechanism.

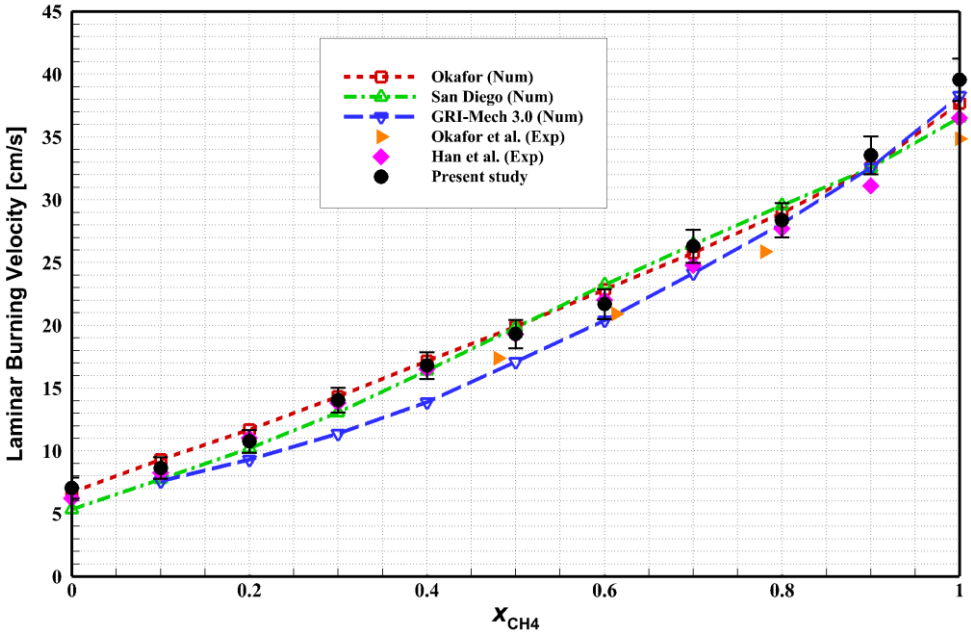

Fig. 5. Comparison between obtained results and other mechanisms

To ensure a grid-independent solution, a minimum of 1000 grid points were used in each case, while the adaptive grid control parameters of GRAD and CURV were determined to vary between 0.03 and 0.05. The results showed that the change in the laminar burning velocity by decreasing the size to GRAD=0.03 and CURV=0.05 is less than 0.1% (Table 1). Therefore, it was selected as the optimum mesh size.

3- 2- 2- Uncertainties

Experimental investigations must include uncertainty as an essential aspect. As mentioned in the literature, there are several uncertainties involved in determining laminar burning velocity using a constant volume chamber [34, 35]. Radiation heat loss is the primary source of uncertainty in the current investigation. As a result, the radiation uncertainty was calculated using a fuel-independent correlation Yu et al. (36)] provided. Radiation effect and, hence, radiation uncertainty rise as flame speed drops. Another potential mistake source is wall confinement. The vessel's diameter (225 mm) is sufficient for capturing flame radii up to 35 mm for the image-processing process. The vessel's wall's induction of little uncertainty due to observed flame radii, which are around 30% of the chamber radii [37]. In radii lower than 10 mm, the change in flame radii over time was not linear due to ignition energy. Flame radii smaller than 10 mm were not used to calculate laminar burning velocity or Markstein length to prevent the ignition energy effect. In outwards propagating flames, buoyancy is a source of uncertainty, especially at low flame speeds [38]. The flame front may be severely deformed as a result of this impact. In the scope of the recorded flame radius in the current study, there was no permissible distortion in the flame structure.

Despite the flame occasionally being displaced upward, Okafor et al. [8] claimed that this event had no impact on the outcomes. Uncertainty analysis also considers the technique for extrapolating unstretched laminar burning velocity. The stretch extrapolation uncertainty was reduced by extracting the unstretched laminar burning velocity using a non-linear technique. The sentences that follow give a more thorough justification for this choice. Ammonia combustion generates a significant amount of water, which might condense in the chamber. Ammonia is soluble in water, therefore this absorption might lead to ambiguity when preparing mixtures. As a result, the chamber was dried with airflow following each experiment. The temperature and pressure sensors have an accuracy of 0.5% FS (full scale), respectively, with full scales of 5.0 atm and 0.4 °C for a range of 100 to 200 °C. For different conditions, uncertainties were calculated and presented with the SL results. For temperature, uncertainty is calculated using Equation (7):

$$u_N = \left[u_c^2 + \left(\sum_{1}^{N-1} u_i^2\right)\right]^{1/2} \quad (7)$$

Which u_c is the instrument error and u_i is the first-order uncertainty. To verify the reproducibility of results, each experiment was run three to four times. An average of the results was then presented. Random or statistical uncertainty [38] is connected to the scatter of recorded

Table 2. Experimental cases

Case	ϕ	LFG Composition	ENH_3	P_i (atm)	T_i (K)
1 (Base case)	1.0	LFG70	0.4	1	300
2	0.7:0.1:1.6	LFG70, LFG50, LFG100	0.4	1	300
3	1.0	LFG70	0.0:0.2:1.0	1	300
4	1.0	LFG 70	0.0:0.2:1.0	1	300
5	1.0	LFG70	0.4	1,3,5,7,10	300
6	1.0	LFG70	0.4	1	300, 323, 373, 423, 473

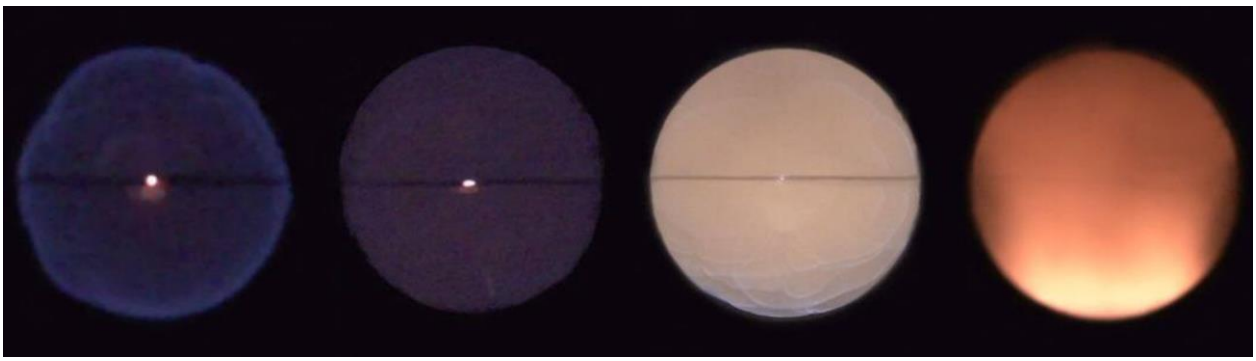

$\alpha = 0$ $\alpha = 0.4$ $\alpha = 0.6$ $\alpha = 1$

Fig. 6. Direct images of ammonia/landfill/air premixed flames for different content of ammonia at Pi=0.1Mpa, φ=1 and T=300 K

results in repeating measurements with similar operational conditions. A 95% confidence level was used to calculate the random uncertainty. In this investigation, the most significant uncertainty for all quantifiable uncertainties was 20.1%. The uncertainty is lower than 10.0% for situations with flame speeds greater than 9.0 cm/s when most of the measured data fall within this range.

The combustible mixture quantities were prepared in the chamber according to the required partial pressures of the component gases using a GE UNIK 50 0 0 silicon pressure sensor (with an accuracy of ± 0.04% full scale).

4- Results and discussion

The present work is mainly focused on investigating the influence of initial temperature, pressure, and various fuel compositions on landfill gas's LBV and fuel compositions. At first, landfill gas lean and rich composition limits are achieved via experimental measurements.

The influence of fuel's CO_2 mole fraction and equivalence ratio on LBV was investigated numerically and experimentally. The range of variation of the investigated characteristic is listed in Table 2.

Where LFG70: $\frac{[CH_4]}{[CH_4]+[CO_2]}=0.7$, $\alpha=\frac{[NH_3]}{[NH_3]+[CH_4]+[CO_2]}$, $\beta=\frac{[CH_4]}{[[CH_4]+[CO_2]]}$ where $[NH_3]$, $[CH_4]$ and $[CO_2]$ are the initial more mole fractions.

4- 1- Flame observation

Direct images of ammonia/landfill/air premixed laminar spherically propagating flame for various conditions are shown in Fig. 6. The chemiluminescence (orange color) was seen from premixed ammonia/landfill/air flames. Hayakawa, Goto [4] have suggested that the appearance of orange chemiluminescence results from the NH_2 ammonia a band spectra [32] and superheated H_2O vapor spectra. As the concentration of ammonia increases, so does the NH_2 level, resulting in a clearer orange chemiluminescence. At larger radiuses, the flame's shape was jellyfish-like. Also, at higher amounts of α, unstretched laminar burning velocity is

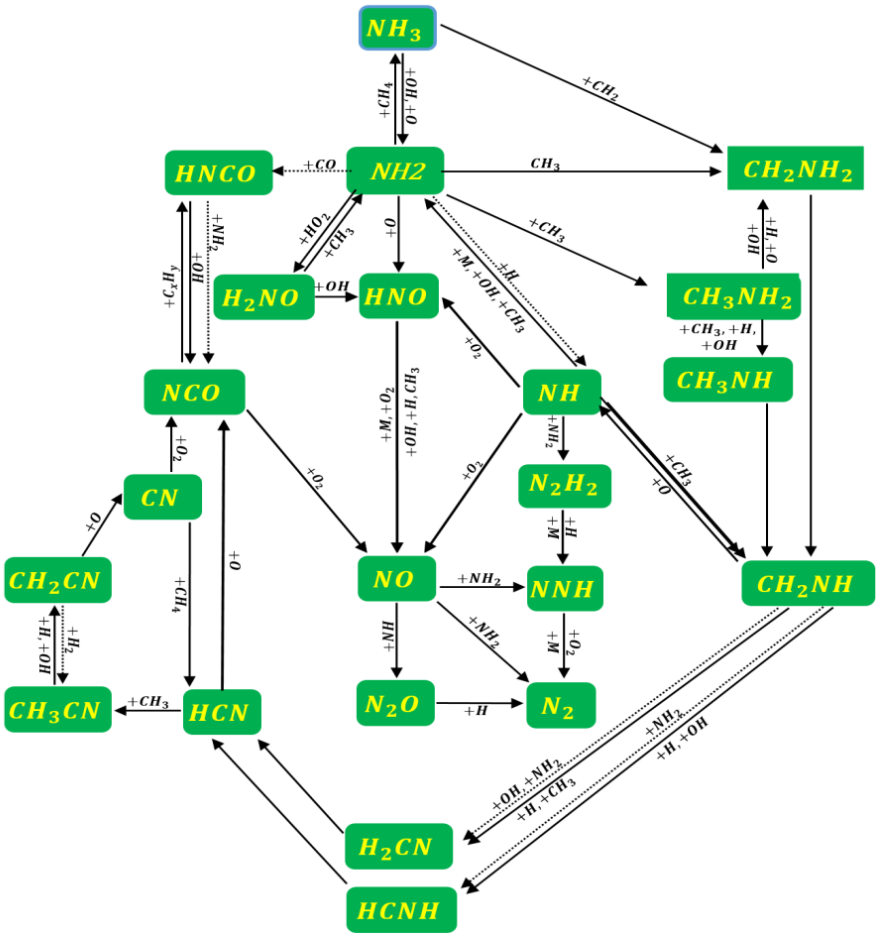

Fig. 7. Reaction path diagram at φ=1 (40)

shallow. Thus, the buoyancy effect is significant and changes the flame shape, especially for this condition.

4- 2- Flame characteristics of landfill/ammonia/air

Flame speed (S_l) increase typically results from thermal, chemical, and transport effects. It was shown in a previous work that the increase of S_l is dominated by the chemical effect, and LBV is positively influenced by the thermal effect (39). The evident growth in the two critical active radicals (*OH* and *H*) peak mole fraction elucidates that the chemical effect is more dominant when the CH_4 mole fraction is higher in the NH_3/landfill flame.

The pollutants and justification of their variation because of methane-ammonia and CH_4/CO_2 mixtures combustion kinetics [40-45] are rendered in this section. To study how emissions are affected by the air content, the mixture chemical kinetics has been investigated under various conditions (Table 2). Fig. 7 represents the reaction paths of different methane-ammonia mixture compositions.

Table 3 lists the corresponding step numbers and elementary reactions involved in the process of enhancement.

4- 3- Flame propagation at different conditions

Ammonia/landfill/air mixtures spherically propagating flames under different conditions based on Table 2. were visualized using Schlieren photography, and the results are shown in Figure 8. Each image is explained in its corresponding section.

4- 4- Examining the pressure effect

In numerous industrial applications, combustion takes place under high pressure. Because of that, the investigation of fuel properties in pressure above the atmosphere is essential.

The Chamber's pressure history *(P)* during the propagation of the flame is shown in Fig. 8-a at φ =1.0 for different pressures. The surface of the flame is very smooth when P_u = 1 (unburned pressure) atm and wrinkled at P_u = 10 atm, which causes flame instability and makes it susceptible to cellular

Table 3. Step number and elementary reaction

Step Number	Elementary Reaction	Step Number	Elementary Reaction
R1	$H + O_2 \rightleftharpoons O + OH$	R12	$OH + CH_3 \rightleftharpoons CH_2(S) + H_2O$
R2	$O + H_2 \rightleftharpoons OH + H$	R13	$HO_2 + CH_3 \rightleftharpoons OH + CH_3O$
R3	$OH + H_2O_2 \rightleftharpoons HO_2 + H_2O$	R14	$HCO + H_2O \rightleftharpoons H + CO + H_2O$
R4	$OH + HO_2 \rightleftharpoons O_2 + HO_2$	R15	$HCO + O_2 \rightleftharpoons H_2O + CO$
R5	$H + O_2 + H_2O \rightleftharpoons H_2O + H_2$	R16	$OH + CH_4 \rightleftharpoons CH_3 + H_2O$
R6	$H + HO_2 \rightleftharpoons O_2 + H_2$	R17	$HCO + M \rightleftharpoons H + CO + M$
R7	$2OH \rightleftharpoons O + H_2$	R18	$H + NO + M \rightleftharpoons HNO + M$
R8	$H + OH + M \rightleftharpoons H_2O + M$	R19	$NH_2 + NO \rightleftharpoons NNH + OH$
R9	$H + CH_3(+M) \rightleftharpoons CH_4(+M)$	R20	$HNO + H \rightleftharpoons H_2 + NO$
R10	$O + CH_3 \rightleftharpoons H + CH_2O$	R21	$NH_2 + H \rightleftharpoons NH + H_2$
R11	$OH + CO \rightleftharpoons H + CO_2$	R22	$NH_2 + O \rightleftharpoons HNO + H$

instabilities [46]. The spherical flame's size became smaller as the mixture's initial pressure increased. It can be deduced that when the mixture's initial pressure increases from 1 to 10 bar, the flame's speed decreases from 16.1 to 6. From two different thermodynamic and kinetic perspectives, this event can be understood.

Diffusivity (mass and thermal) and bulk movement are the two crucial parameters that influence the LBV, and the former becomes dominant when the pressure is increased. The coefficient of thermal diffusivity is defined by equation 8. Only using Chapman–Enskog theory [47] expresses the mass diffusion coefficient's dependence on the pressure and temperature in equation 9. In which different indices refer to various molecules in the mixture, molar mass (g/mol) is represented by M, absolute temperature (K) is characterized by T, $\sigma_{12} = 0.5(\sigma_1 + \sigma_2)$ is the average collision diameter, T represents temperature-dependent collision integral, and is dimensionless. As it is shown in these equations, there is an inverse relation between diffusivity and pressure. Thus, mass and thermal diffusivity coefficients will decrease when pressure increases, directly affecting fuel's burning rate. Fuel's burning rate represents its coefficient of thermal and mass diffusivity. Consequently, as the pressure rises, the LBV will be decreased.

Thermal diffusivity:

$$\alpha = \frac{k}{\rho_u C_p} = \frac{kR_uT_u}{P_uC_p} = f(k, R_u, C_p) \times \frac{T_u}{P_u} \quad (8)$$

Mass diffusivity:

$$D = \frac{1.858 \times 10^{-3} \times T_u^{1.5} \times \sqrt{\frac{1}{M_1} + \frac{1}{M_2}}}{P_u \sigma_{12}^2 \Omega} = f(M, \sigma, \Omega) \times \frac{T_u^{1.5}}{P_u} \quad (9)$$

Although increasing pressure increases reaction rate, the primary reason for reducing laminar burning velocity versus elevated pressure is the higher density of the un-burned mixture. Physically, there is a dense gas above that the flame passes through and heats up.

From a kinetic perspective, chemical reactions increase as the pressure increases. It is deduced by scrutinizing Fig. 9-a that the pressure substantially influences the radical pool level (high pressure→low radical). Therefore, it is expected that a reduction in radicals leads to a decrease in laminar burning velocity.

As is shown in Fig. 9-b, when pressure is increased, *NO* (nitrogen monoxide) formation is decreased. Le Châtelier's principle states that the equilibrium goes toward neutralizing change [48]. Therefore, with the increase of pressure, the system moves toward decreasing the mole number. *NO* formation decrease is expected due to the following reaction.

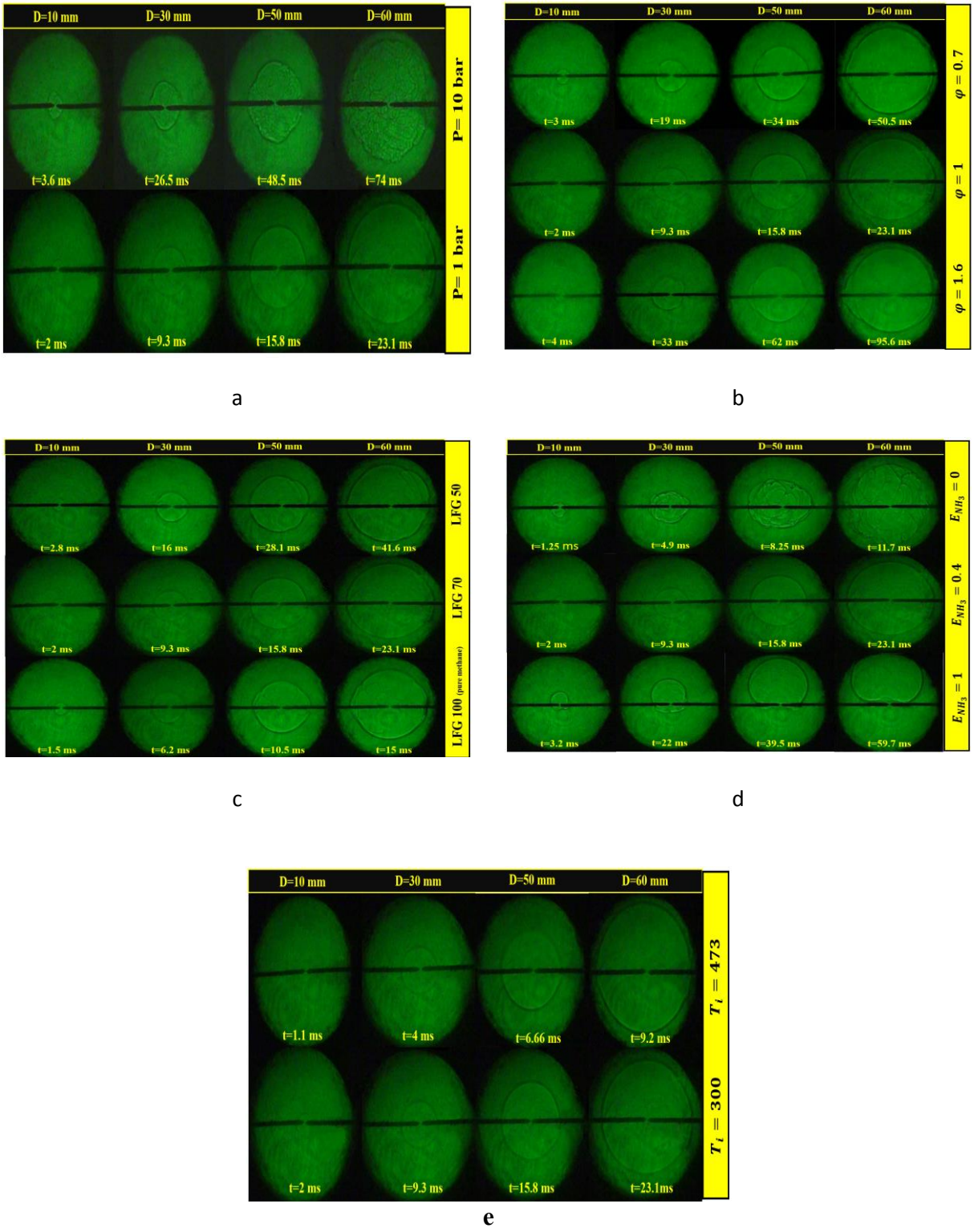

Fig. 8. Flame propagation images at different: a) pressure, b)equivalence ratio, c) carbon dioxide content, d) ammonia content and e) initial temperature

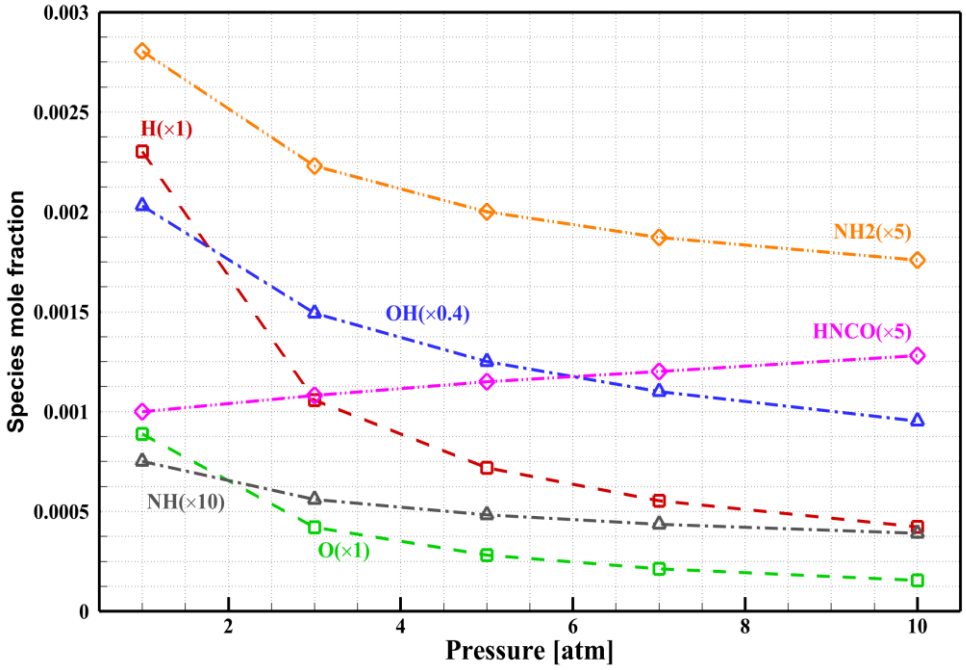

a

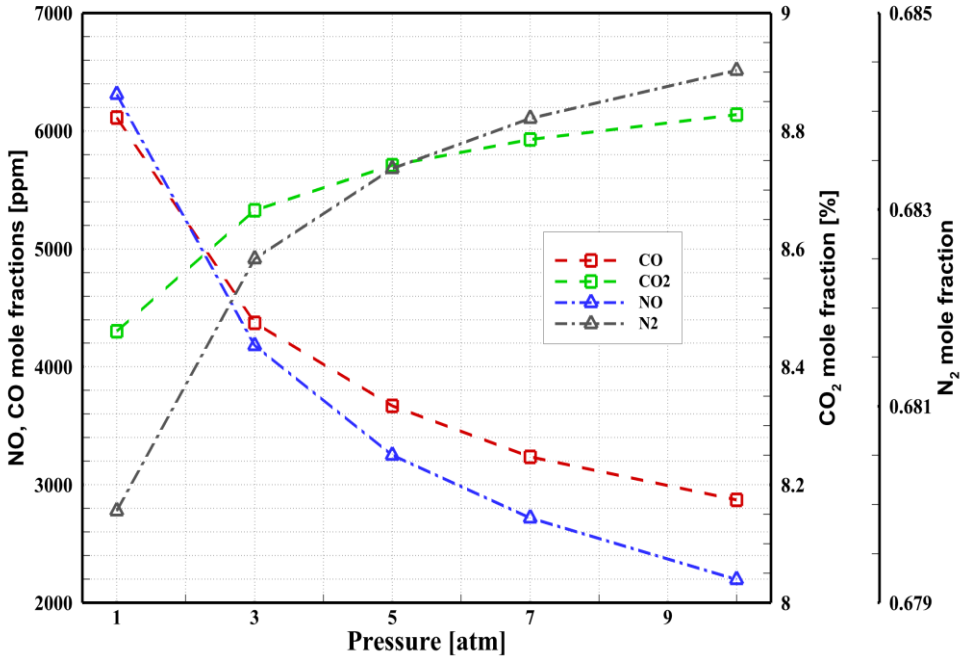

b

Fig. 9. Measured and Simulated radicals and emissions for different pressure at α=0.4,β=0.7,φ=1 and T=300K

Table 4. Comparison of experimental and numerical results under different pressure

	Exp.	Num. (Okafor)	Num. (GRI-Mech 3.0)	Num. (San Diego)
1	16.1	16	13.5	15.7
2	10	10.4	8.8	9.6
3	8	8.6	7.3	8.2
4	6.9	7.7	6.5	7.4
5	6	6.9	5.7	6.4

$$4NH_3 + 5O_2 \rightleftarrows 4NO + 6H_2O \quad \text{(R23)}$$

Because ammonia and ammonia blends are proposed as a stepping stone toward a future carbon-free industry, it is crucial to have an insight into other essential emissions such as *CO* (carbon monoxide) and CO_2. Similarly, *CO* declines, and CO_2 intensifies as the pressure increases.

$$2CO + O_2 \rightleftarrows 2CO_2 \quad \text{(R24)}$$

Due to the high reactivity of NH_3 than CO_2, NO change is much more than *CO* and CO_2.

At lower radicals' pool level and elevated pressure, *NO* is expected to vary more than *CO* and CO_2 since the reactivity of NH_3 is higher than CO_2. Regarding the decrease of pool level of radicals due to the increase of pressure, *CO* is expected to become dominant, reinforcing the *HNCO* pathway as is shown in Fig. 7. To that end, *CO* is consumed by other species, which can cause *CO* levels to decrease. On the contrary, Fig. 9-b states a negligible increase in CO_2 levels. As mentioned above, the pool level of radicals decreases with the increase in pressure; thus, CO_2 can hardly react with methane or ammonia to produce *OH* radicals. Therefore, most of it remains in the form of CO_2.

As is shown in Fig. 10-a, the maximum obtained flame temperature increases from 2102 to 2143 K by the increase of pressure from 1 to 10 bar due to the interaction of species. It is expected that increasing pressure increases concentration, leading to the chemical effect. As a result, adiabatic flame temperature increases when pressure rises.

As shown in table. 4, although pressure rise leads to an increment of the reaction rate, the main reason for decreasing laminar burning velocity with pressure is higher values of unburned mixture density. Physically, there is a denser upstream gas for the flame to pass through and heat up.

Fig. 10-b shows the LBV sensitivity of the ammonia/landfill mixture for elevated initial pressure. As initial pressure rises, the effect of chain-terminating reactions (R4, R8, and R20) also increases. The enhancement of such reactions is a reason for the depletion of the radical's pool and consequently, a decrease in LBV. The error bars shown in Fig. 10-a represent the level of uncertainty associated with flame speed. By increasing the pressure, flame speed decreases non-linearly.

Fig. 10-b depicts the normalized sensitivity coefficient of the laminar combustion velocity of NH3/Landfill at different pressures. The sensitivity coefficient, which demonstrates how flame speed changed in response to a perturbation in the ith reaction, is computed using Equation 10:

$$SF_i = \frac{\alpha_i \partial s_l}{s_l \partial \alpha_i} \quad (10)$$

Where SF is the sensitivity coefficient for the ith reaction is, α_i is the rate constant for the ith reaction, and s_l is the laminar combustion velocity.

The positive sensitivity coefficient indicates a direct correlation between the laminar burning velocity and the reaction, whereby an increase in one leads to a corresponding increase in the other.

The impact of chain-terminating reactions (R3, R4, and R9) grows as initial pressure rises. The increase in these reactions is what causes the pool of radicals to be depleted, which leads to a reduction in LBV.

4- 5- Examining the equivalence ratio effect

Fig. 8-b shows the recorded Schlieren images of the spherically propagating flames of NH_3/landfill/air mixtures at different equivalence ratios. Generally, accelerated flame propagation can effectively alleviate the buoyancy effect (5)]. Ronney and Wachman (38)] reported that the effect

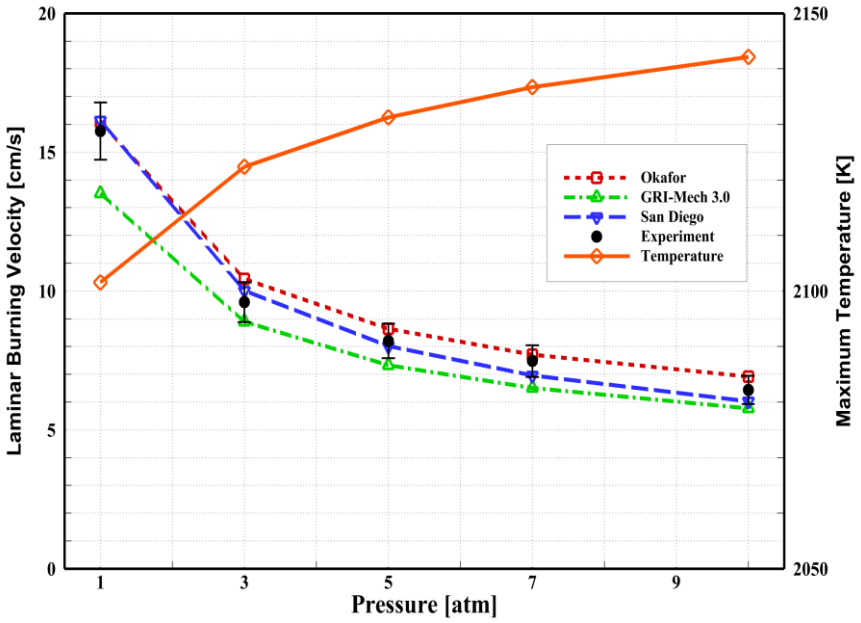

a

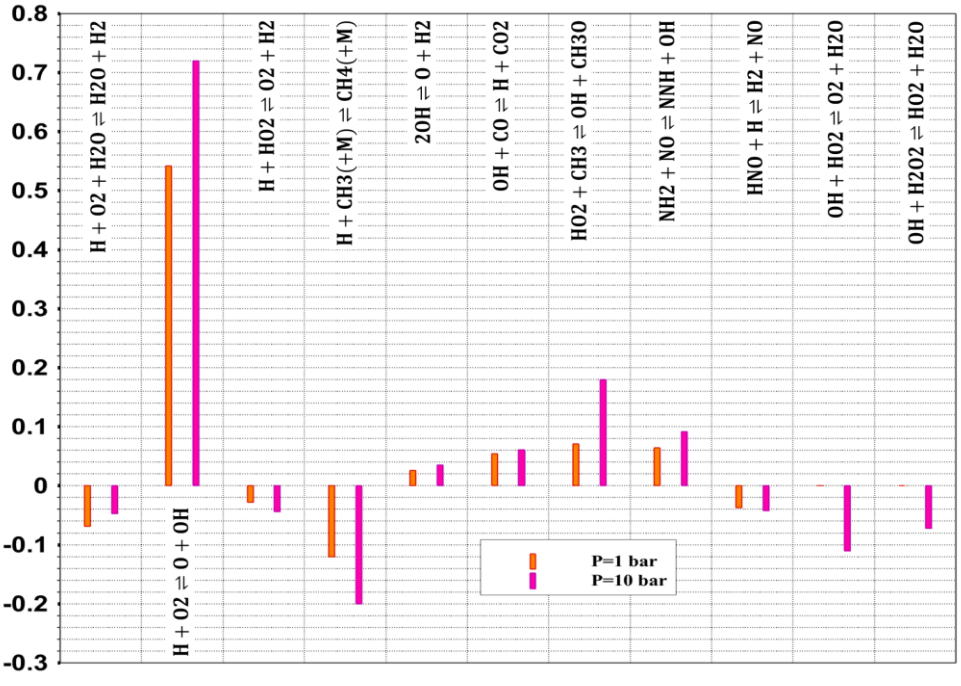

b

Fig. 10. Measured and simulated flame speed and maximum flame temperature for different pressure at α=0.4,β=0.7,φ=1 and T=300K

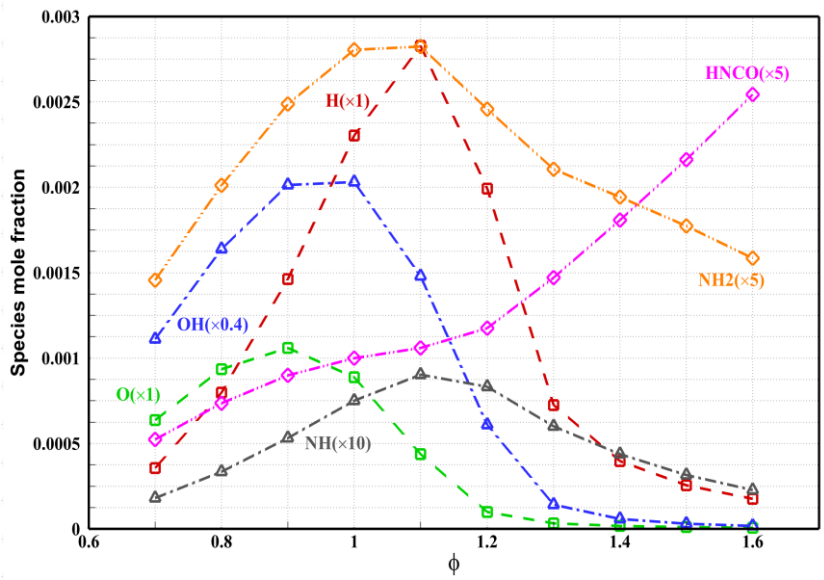

a

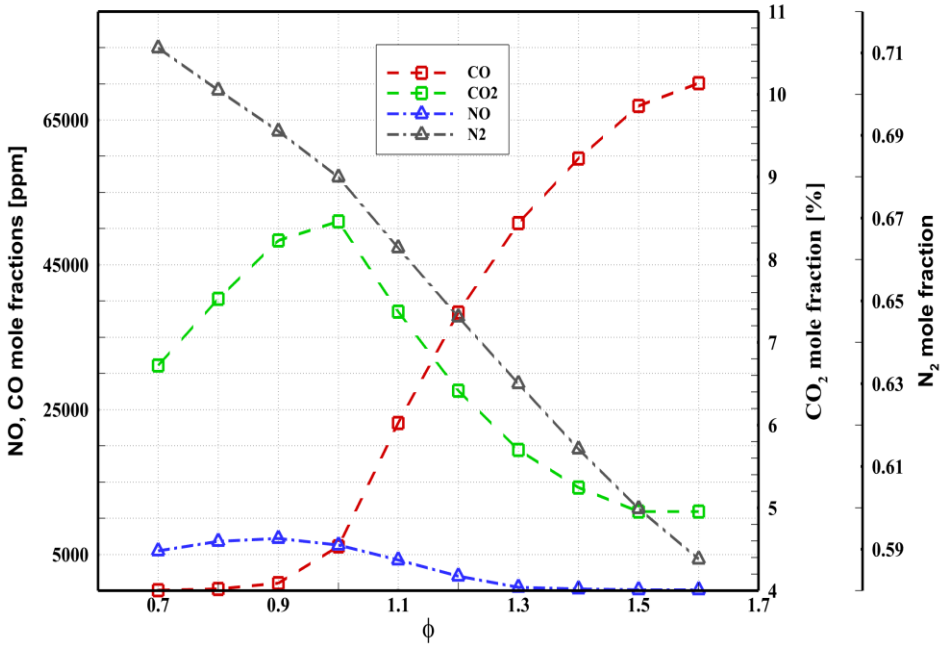

b

Fig. 11. Measured and simulated radicals and emissions for different equivalence ratios at α=0.4,β=0.7,P=1 bar and T=300K

Table 5. Comparison of experimental and numerical results under different equivqalence ratio

φ	Exp.	Num. (Okafor)	Num. (GRI-Mech 3.0)	Num. (San Diego)
0.7	8.1	8.5	6.4	8.8
0.8	11.1	11.9	9.6	12.6
0.9	13.9	14.6	12.1	15.2
1.0	15.7	16	13.5	16.1
1.1	15.1	15.2	12.7	14.9
1.2	11.5	11.8	9.8	11.5
1.3	8.1	8.5	7.9	8.8
1.4	7.5	6.8	6.6	7.2
1.5	6.3	5.6	5.6	6
1.6	5.4	4.7	4.8	5

of buoyancy on S_L becomes notable for flames with SL less than 15 cm/s. Thus, the buoyancy effect mainly affects NH_3/Landfill/air mixtures SL measurements. Flame edges in the case of φ = 0.7 to 1.6 were clearly observable, so the equivalent flame radius was relatively easy to calculate. Yet, in the case of φ lesser than 0.7 and higher than 1.6 the bottom boundary of the flame was not entirely clear.

The three most essential reactions that produce *OH* radicals are reactions between (NH_3+O2), (CH_4+O_2), and (CO_2+*H*). Therefore, the peak value of *OH* concentration in stoichiometric conditions can be justified because fuel and oxygen have a complete reaction under such conditions. Incomplete combustion leads to lower *OH* concentration than stoichiometric. Based on the argumentations above, intermediate radicals (*O*, *OH*, and *H*) have a crucial role in the chemical effect. These radicals enhance the chemical reaction level, which causes the LBV to increase.

Besides, due to the insufficient oxygen in rich flames, $NH_2 + NH = N_2H_2 + H$ promotes the production of H radicals in rich flames, which significantly influences the S_L of rich flames. It should be noted that the combination reactions of NH_i are favored in the rich flame. N_2H_2 has a considerable impact on the S_L, mainly produced by the reaction of NH_2 with *NH* (NH_2+*NH*=N_2H_2+*H*) or self-recombining (NH_2+NH_2=N_2H_2+H_2) [7].

As is shown in Fig. 12-b, the most basic reaction R1 is capable of increasing laminar burning velocity. Despite *H* radical being destroyed, *OH* and *O* radicals are generated by R1, which dramatically increases chemical reactivity. Laminar burning velocity of the Landfill/ammonia/air mixture is linearly connected with *H* radical. Inhibitory reaction is R9. The chemical reactivity is reduced due to the significant consumption of *H* radical by R9.

The fact that a lot of oxygen and hydrogen radicals are consumed by R5 and R10 justifies the faster drop in laminar burning velocity under lean conditions.

As is shown in Fig. 12-a, the temperature's peak value occurs around the stoichiometric condition. Additional analysis of temperature diagrams reveals that the lower peak temperature corresponds to the phase of lean-burn combustion. This finding is consistent with the notion that, as oxidizer concentration increases, a significant amount of the energy from combustion is utilized in preheating the excess air. Besides, in rich conditions, the combustion process is incomplete because of inadequate oxygen. The generated heat is consumed to preheat unburnt species. Thus, the maximum temperature in the rich condition is expected to be lower than the stoichiometric one (Table 5).

4- 5- 1- Under the rich conditions

It is understood that more *CO* is generated in fuel-rich conditions than in lean combustion. This trend can be attributed to CO_2 concentration being much higher than the O_2 in the rich mode. Thus, it is more plausible for CO_2 to react with the hydrogen radicals produced from the city gas or ammonia reactions to produce *CO* even in medium temperatures (48, 49)]. The mentioned reaction generates *CO* and *OH* as below:

$$CO_2 + H \rightarrow CO + O \qquad \text{(R25)}$$

Both the rich condition and *OH* and CH_3 radicals are at higher levels in this mode. This condition would strengthen the change of NH_3 and NH_2 conversion to CH_2NH, which results in more *HCN*. The Andrussow process suggests that

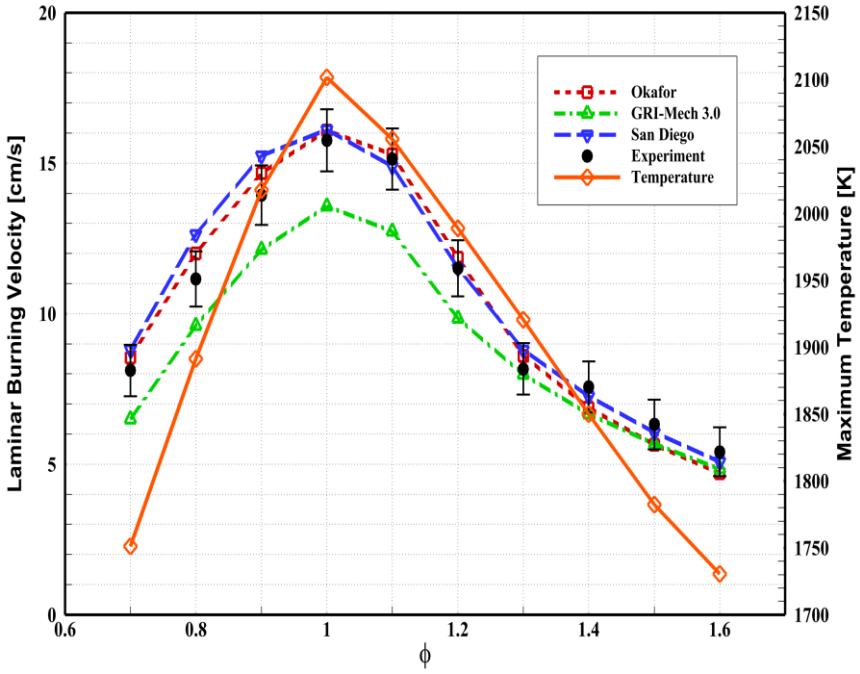

a

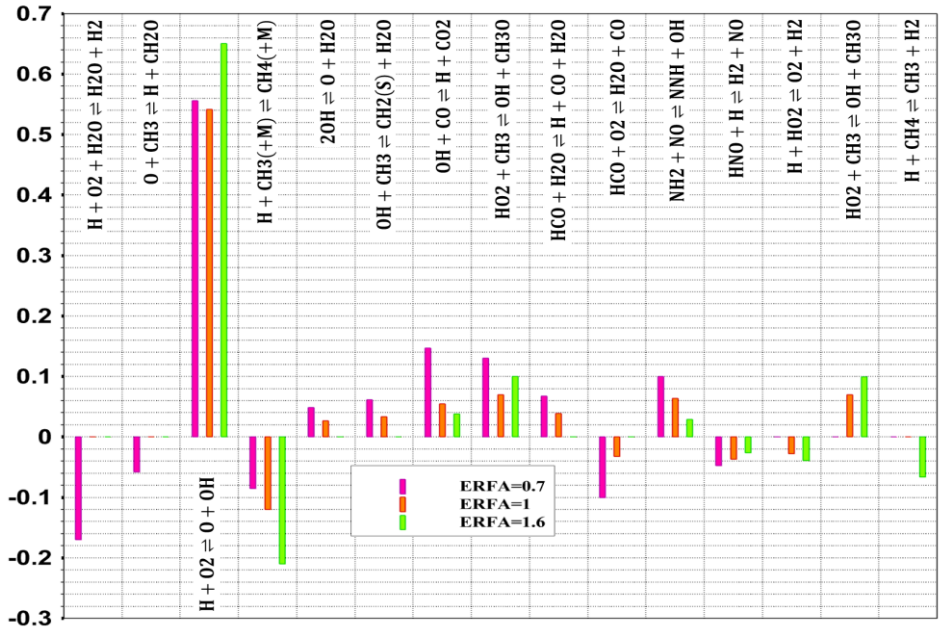

b

Fig. 12. measured and simulated flame speed and maximum flame temperature for different equivalence ratios at α=0.4,β=0.7,P=1 bar and T=300K

the generation of *HCN* is primarily dominated by a specific route due to the high level of exothermicity involved. In other words, regardless of the circumstances, the *HCN* generation route remains more dominant than alternative routes, owing to the fact that it is very exothermic (with a change of enthalpy equal to −240 kJ/mol) [50].

$$2CH_4 + 2NH_3 \rightleftharpoons 2HCN + 6H_2O \quad \text{(R26)}$$

Under rich conditions, both *CO* and *HCN* are known to increase. In addition, the absence of sufficient oxygen content may result in a conversion of some *HCN* molecules to *NCO* or *HNCO*, as illustrated in the following equations:

$$\begin{matrix} HCN \xrightarrow{+CH_3} CH_3CN \xrightarrow{+H,+OH} \\ CH_2CN \xrightarrow{+O} CN \xrightarrow{CH_4} HCN \end{matrix} \quad \text{(R27)}$$

$$HCN \xrightarrow{+O} NCO \xrightarrow{+C_xH_y} HNCO \quad \text{(R28)}$$

When compared to other scenarios, the emission concentration of *CO* and *NO* is lower in the rich mode. This occurrence can be attributed to the lower concentration of oxidizers leading to a decrease in the content of radical pool (*O*, *H*, and *OH*) and an increase in the concentration of *CO*. However, the rich condition produces a greater quantity of *CO*, which exhibits high reactivity with NH_2, leading to a decrease in *NO* production via the consumption of NH_2 molecules, as seen in the following reaction:

$$CO + NH_2 \rightarrow HNCO + H \quad \text{(R29)}$$

The analysis of the combustion kinetics highlights that a lower amount of CO_2 is generated during the rich combustion process relative to the stoichiometric one. This finding is understandable as the complete combustion reaction occurs when the mixture fuel is under stoichiometric conditions, which results in a higher concentration of CO_2 compared to the rich-fuel conditions.

4- 5- 2- Under the lean condition

Fig. 11-b demonstrates that the concentration of *NO* is lower in the rich burn state than in the lean-burn condition but higher in the stoichiometric state. The increased amount of O_2 molecules in the lean-burn combustion causes this variation. The highly reactive O_2 molecules prevent the CO_2 molecules from reacting with hydrocarbons or ammonia, leading to the rapid conversion of ammonia to *NO* through the reaction chain below [7]:

$$NH_3 \xrightarrow{+O,+OH} NH_2 \xrightarrow{+O} HNO \xrightarrow{+O_2,+M} NO \quad \text{(R30)}$$

Under lean-burn conditions, the formation of *NO* is significantly impacted by the presence of *HCN* radicals, which can be converted into *NO* via a chain of reactions that are more likely to occur when oxygen concentrations are high. The series of chain reactions involved in this process are as follows;

$$\begin{matrix} HCN \xrightarrow{+CH_3} CH_3CN \xrightarrow{+H,+OH} \\ CH_2CN \xrightarrow{+O} CN \xrightarrow{O_2} NCO \xrightarrow{+O} NO \end{matrix} \quad \text{(R31)}$$

Also, the temperature of the flame in lean and especially in the stoichiometric conditions is higher than in rich mode, which results in the more thermal formation of *NO* in lean and stoichiometric conditions. Also, the amount of *CO* produced in lean-burn mode is much lower compared to the stoichiometric and rich conditions. Under the lean condition, Methane has a higher reactivity in comparison to CO_2. Thus, methane wins the competition to react with oxygen, leading to higher carbon dioxide emissions. Also, the fuel mixture contains CO_2 itself, and this causes a synergy effect in CO_2 amounts. In this situation, by moving toward rich conditions (low oxygen), CH_4 has an incomplete combustion process, leading to more *CO* and less CO_2.

In addition, the lean-burn condition features lower concentrations of *CO*, which increases the likelihood of NH_2 molecules reacting and generating *HNO* (the most crucial radical involved in *NO* formation). The reduced levels of *CO* also mean that more ammonia radicals (NH_2) are available to react, enabling the conversion of *NO* molecules to N_2.

4- 6- Examining the fuel composition effect

Schlieren photography for ammonia/landfill/air premixed spherically propagating flame at various fuel compositions was carried out, and the results are shown in Fig. 8-c and d. The time needed for reaching a certain radius was decreased, i.e., the flame propagating speed increased by the ratio of ammonia in the mixture (α). Wrinkles at the flame front could be observed in the cases in which the landfill ratio was above $\alpha = 1$ (pure methane). It was the Diffusive-thermal instability that induced the wrinkles. It is at the high landfill ratios that the flame front wrinkling is observed compared to NH_3/air mixtures' spherically propagating flames that exhibit an intense buoyancy effect [4, 5]. Yet, the flame surface's excellent sphericity shows that buoyancy does not affect NH_3/landfill/air flames strongly, which means flames of NH_3/landfill/air can propagate faster than flames of NH_3/air.

4- 6- 1- Landfill

As shown in Fig. 13-a, with the introduction of CH_4 into the NH_3/LFG/air flame, the peak mole fractions of *OH*, *H*, and *O* radicals experience a notable increase. Pool radical concentration also increases with CH_4 addition. NH_3/LFG/air flames' LBV increases as the CH_4 content in the LFG increases (as is shown in Fig. 14). It is the thermal, chemical,

or transport effects that primarily increase S_l.

With respect to the quantities of emitted emissions (Fig. 13-b), it can be inferred that CH_4 increment has little effect on emissions. There was a marginal rise in the emission of *CO* and *NO* pollutants, while a decline in CO_2 emissions was detected.

Elevated levels of CH_4 in landfills amplify the *OH* radical pool, leading to a boost in the production of CH_2NH molecules (as demonstrated in Fig. 7). Given that the *OH* concentrations surpass those of *O* and *H* radicals, it is plausible that the chain reactions will persist in the following manner:

$$CH_2NH \xrightarrow{+H,CH_3,+OH,NH_2} H_2CN \rightarrow HCN \quad \text{(R32)}$$

$$CH_2NH \xrightarrow{+NH_2,+H,+OH} HCNH \rightarrow HCN \quad \text{(R33)}$$

HCN molecules are reinforced to produce *NO* when the concentration of *O* radicals and O_2 molecules is high. The lower the CO_2 or, the higher the CH_4, the fewer reaction moves in the cyanide direction. Thus, elevating the CO_2 levels leads to a decline in the reaction rate of the cyanide pathway. CO_2 decreases by increasing methane in LFG, as illustrated in Fig. 13-b. The reason for this trend is that even though a higher concentration of methane in the mixture (under stoichiometric conditions) results in increased CO_2 emissions, the reduction of CO_2 in the LFG has a greater impact. Also, a little increase in *CO* concentration. The primary source of *CO* formation in such conditions is:

$$CO_2 + H \rightleftharpoons CO + OH \quad \text{(R34)}$$

It is expected that $CO_2$with *H* abstraction of CH_4 leads to a slight increase in *CO* because of the high reactivity of CH_4.

As the amount of CH_4 increases leads to producing large quantities of energy; on the other hand, less CO_2 concentration in the mixture results in less absorbing the generated heat of CH_4 oxidation. Therefore, the maximum flame temperature increases.

4- 6- 2- Ammonia

NH_3 addition ratio determines its burning rate. In the cases with higher and lower S_L (29.4 cm/s, and 7.2 cm/s), the addition ratio of NH_3 goes to zero and one, respectively (Table 6). This phenomenon can be examined from both thermodynamic and kinetic perspectives. From a thermodynamic standpoint, the increase in flame speed with a decrease in ammonia concentration can be justified by the fact that reduction in ammonia concentration leads to decrease in flame temperature, thereby reducing flame propagation. On the other hand, from a kinetic perspective, reactions and radicals take precedence. Ammonia addition results in radicals' pool decreasing. In other words, since ammonia has a lower LBV, the mixture's LBV is pulled down by the rising concentration of ammonia in the fuel mixture. Because it generates a significant amount of substantial radicals (*O*, *OH*), R5 is crucial for chain branching in all NH_3 mole fractions.

According to the reaction paths shown in Fig. 7, enhancing the ammonia concentration declines the CH_4 concentration in the mixture. As methane is the sole carbon source that generates carbon dioxide, its decline results in a decrease in CO_2 concentrations (Fig. 15-b).

$$CO_2 + H \rightleftarrows CO + OH \quad \text{(R35)}$$

When the concentration of ammonia is high, CO_2 concentration is low. As a result, lower CO_2 produces lesser *CO*.

It can be guessed that the cyanide pathway is a dominant pathway before the turning point ($\alpha = 0.4$), while other pathways except R14 help to produce *NO* formation. This issue can be justified by adding ammonia to the mixture resulting in lower radicals' pool (*O*, *OH*, and *H*) made by the mix due to weaker methane chemical bonds than ammonia.

It is evident from Fig. 15-b that increasing the concentration of ammonia in the fuel mixture (up to $\alpha = 0.4$) first increases *NO* emission, then decreases it after ($0.4 < \propto < 1$). It should be mentioned that four paths have vital roles in generating *NO*.

$$NH_3 \xrightarrow{+O,+OH} NH_2 \xrightarrow{+CO} HNCO \xrightarrow{+OH,+NH2} NCO \xrightarrow{+O2} NO \quad \text{(R36)}$$

$$NH_3 \xrightarrow{+O,+OH} NH_2 \xrightarrow{+\mathrm{H},+\mathrm{OH}} NH \xrightarrow{+NH2} N2H2 \xrightarrow{+H} NNH \xrightarrow{+O2} N2 \quad \text{(R37)}$$

$$NH_3 \xrightarrow{+O,+OH} NH_2 \xrightarrow{+O} HNO \xrightarrow{+O_2,+M} NO \quad \text{(R38)}$$

$$HCN \xrightarrow{+CH_3} CH_3CN \xrightarrow{+H,+OH} CH_2CN \xrightarrow{+O} CN \xrightarrow{O_2} NCO \xrightarrow{+O} NO \quad \text{(R39)}$$

According to Fig. 16-a, it can be understood that there is a turning point around $\alpha = 0.4$. This trend of temperature variations is deduced by the switching mechanisms from the N_2 (nitrogen) route to the *NO* route. However, the reaction pathway for N_2 production began to prevail after the turning point.

Maximum flame temperature is decreased from 2148 to 2055 K by increasing NH_3 concentration from 0 to 1 in the mix, as shown in Fig. 16-a. The combustion enthalpy of ammonia is lower than landfill which results in a lower heat release. As a result, more products lead to lower maximum

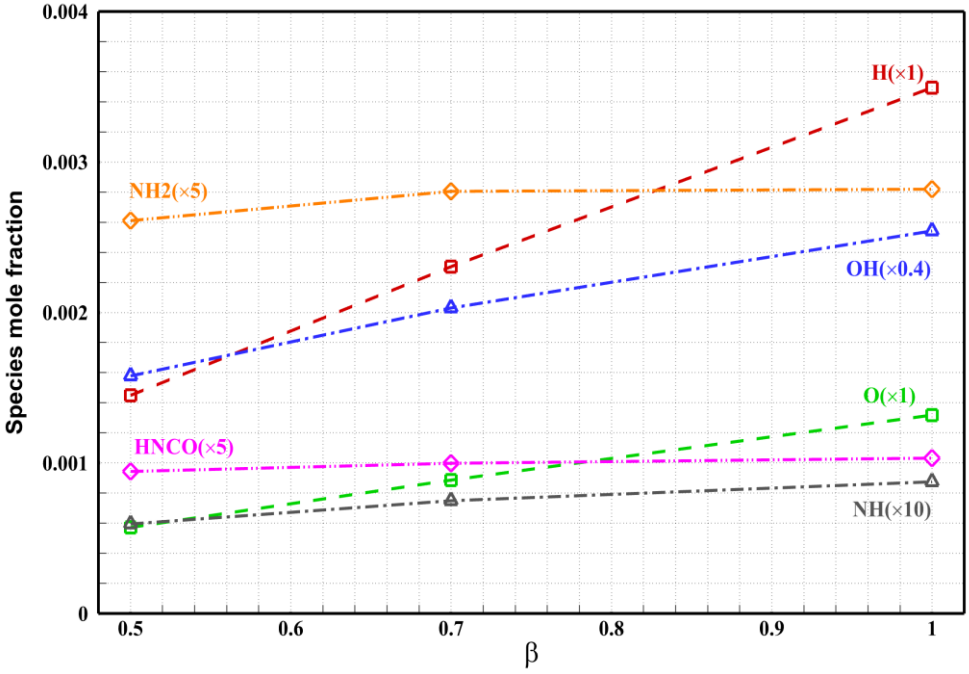

a

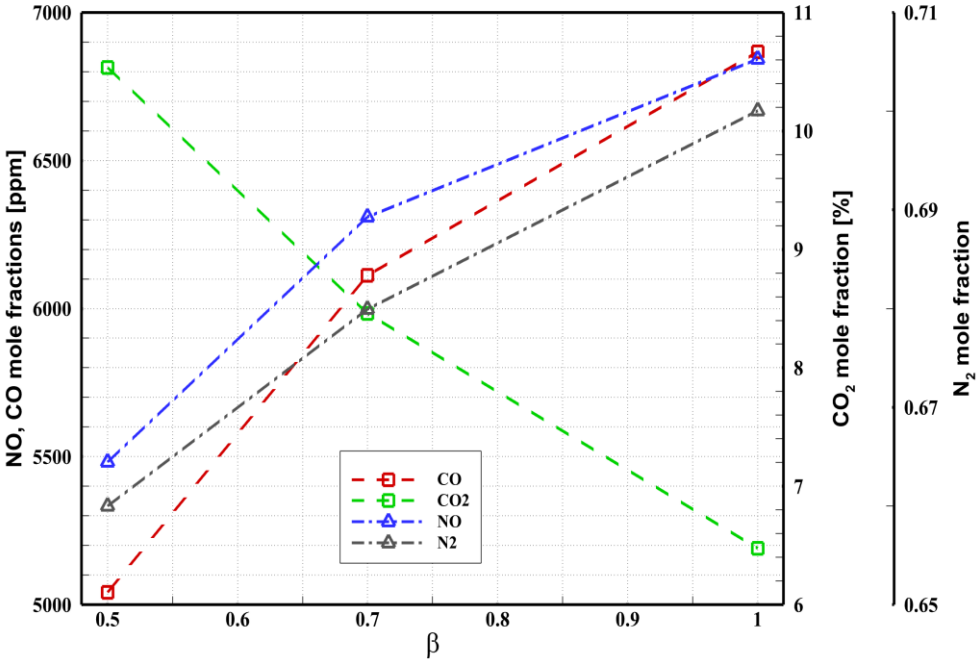

b

Fig. 13. Measured and simulated radicals and emissions for different CO2 content at β=0.7,P=1 bar,φ=1 and T=300K

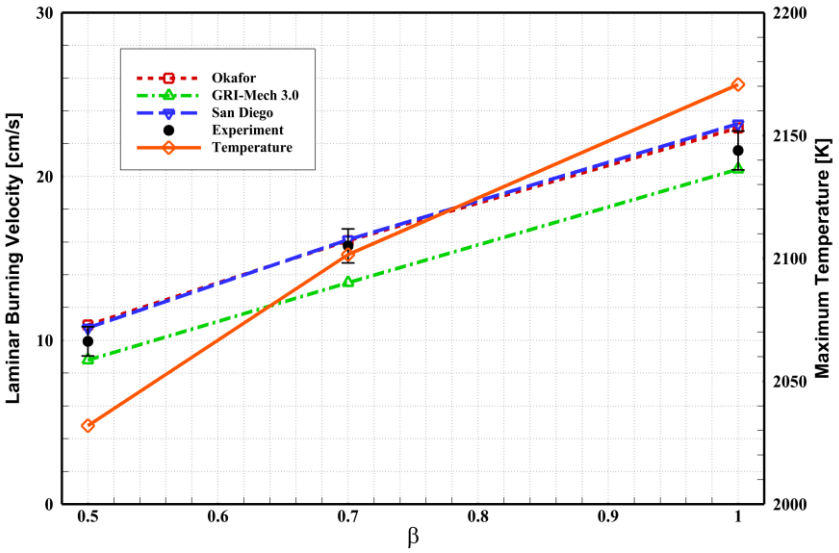

a

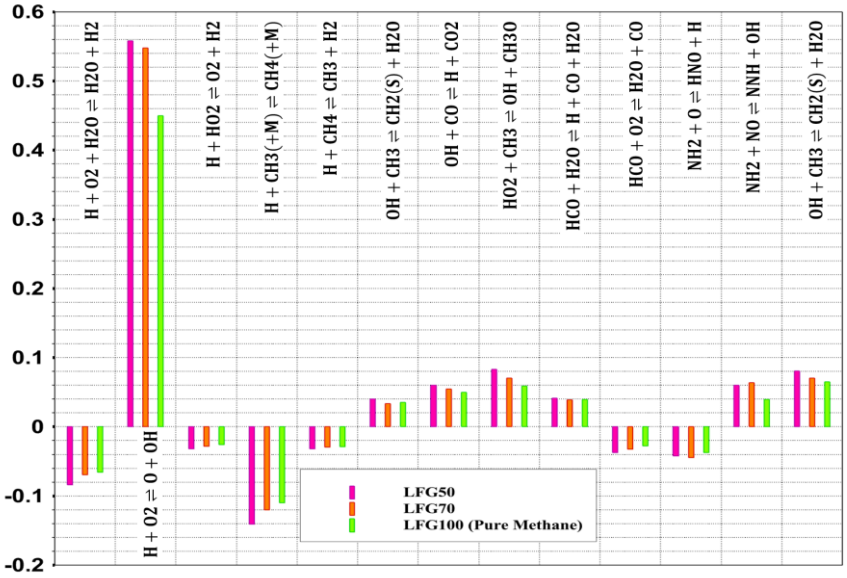

b

easured and simulated flame speed and maximum flame temperature for different CO_2 content at β=0.7, φ=1 and T=300K

Fig. 14. measured and simulated flame speed and maximum flame temperature for different CO2 content at β=0.7,P=1 bar, φ=1 and T=300K

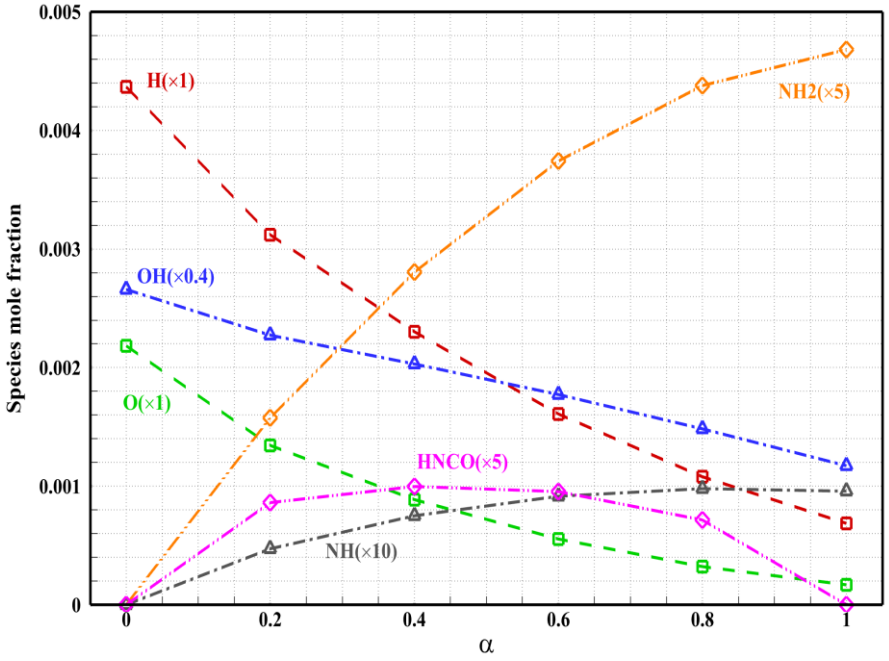

a

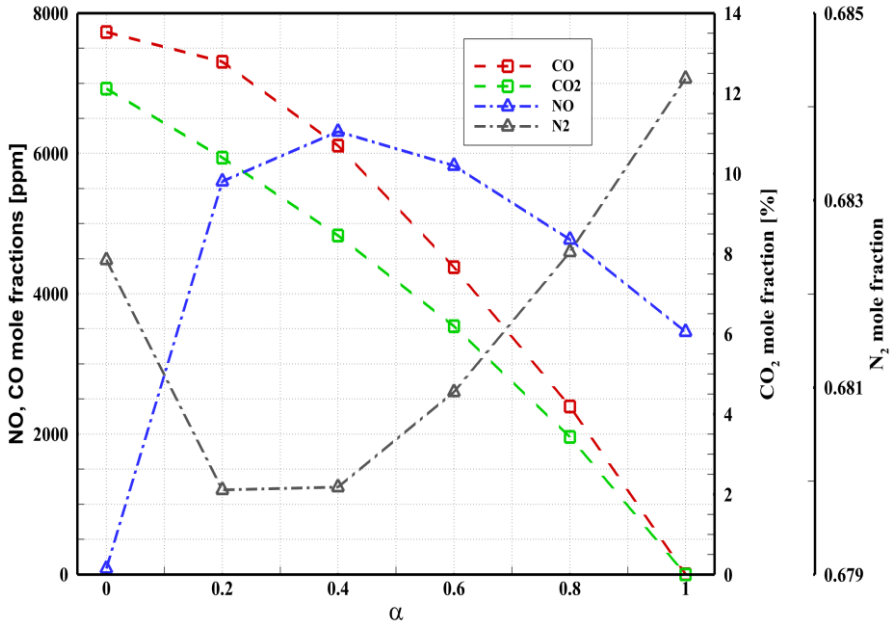

b

Fig. 15. measured and simulated radicals and emissions for different ammonia content at α=0.4,P=1 bar,φ=1 and T=300K

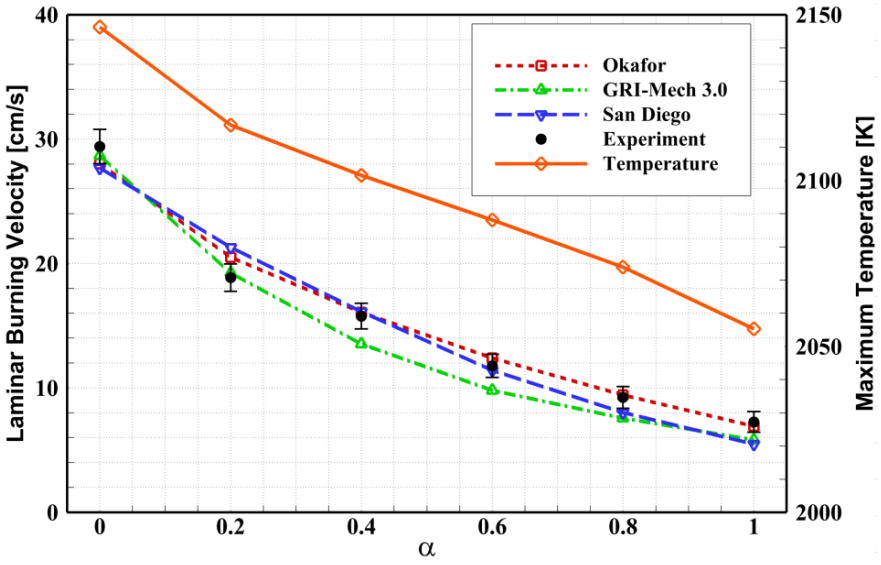

a

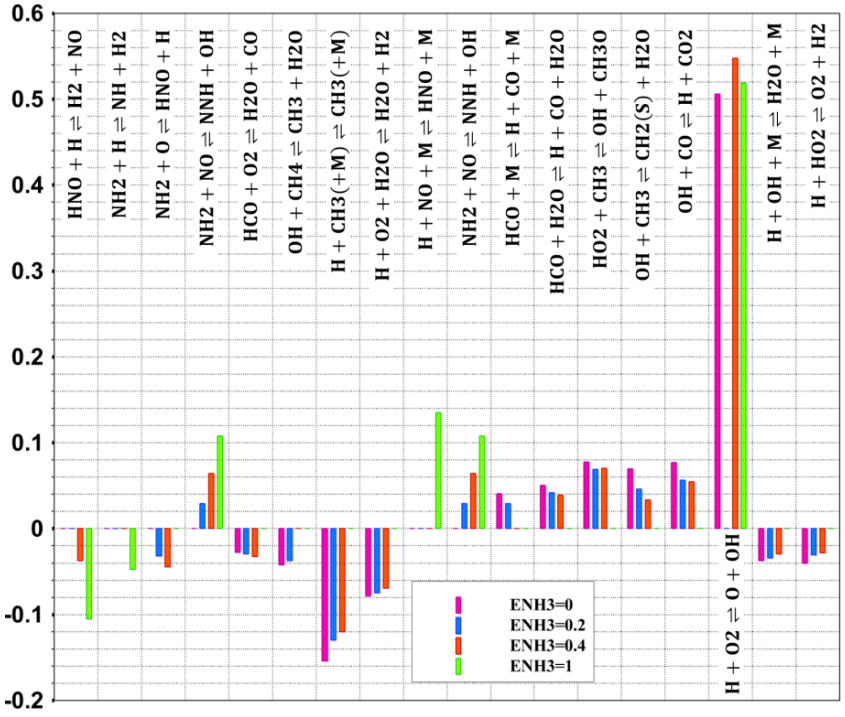

b

Fig. 16. Measured and simulated flame speed and maximum flame temperature for different ammonia content at α=0.4,P=1 bar,φ=1 and T=300K

Table 6. Comparison of experimental and numerical results under different ammonia content

x_{NH_3}	Exp.	Num. (Okafor)	GRI-Mech 3.0	San Diego
0	29.4	28	28.6	27.6
0.2	18.8	20.5	19.2	21.3
0.4	15.7	16	13.5	16.1
0.6	11.7	12.3	9.8	11.4
0.8	9.2	9.4	7.5	8
1	7.2	6.9	5.8	5.4

flame temperature.

As the ammonia content rises, nitrogenous reactions, such as R18 and R19, have larger values of sensitivity coefficients than carbon containing reactions, such as R11 and R12, in the case of reactions with a positive influence on LBV.

Similar to this, reactions like R9 and R5 have considerable deleterious consequences at low ammonia concentrations. R20 and R21 also start to play a bigger role in high ammonia mole fractions.

Most of the time, reactions with positive sensitivity coefficients consume one active radical (*H*, *O*, or *OH*) and make another active radical, whereas reactions with negative effects consume active radicals to produce stable intermediates.

4- 7- Examining the initial temperature effect

Schlieren photography results of ammonia/landfill/air premixed spherically propagating flames are shown in Fig. 8-e for initial temperatures of 300 and 473 K, respectively. With an increase in the initial temperature of the mixture, T_i, the required time for reaching a certain flame radius, Rsch, decreased at the same landfill ratio and flame radius. In other words, the speed of flame propagation increased with the initial mixture temperature increase. Moreover, with the rise in initial mixture temperature, the number of flame front wrinkles decreased.

NH_3/landfill/Air mixtures measured S_l at Ph_i=1, P_i=1, LFG70, $\alpha = 0.4$, T_i = 300~473 K is shown in Table 7. S_l almost increases linearly with Ti increasing. There is an apparent temperature dependence for the NH3/landfill/air flame. Previous studies have shown that the temperature dependence can be expressed by Eq. (10) (51, 52)].

$$\frac{S_L}{S_L^0} = \left(\frac{T_i}{T_i^0}\right)^{\alpha_T} \tag{11}$$

Where $T0_i$ = 298 K, $S0_L$ is the laminar burning velocity at T_i = 300 K. αT is the temperature coefficient reflecting the temperature dependence.

From a kinetic point of view, preheating provides energy and weakens the bonds. It also increases the radical pool (*O*, *H*, and *OH*) (Fig. 17-a).

The positive sensitivity coefficient is larger for $H+O_2=O+OH$ and $HO_2+CH_3=OH+CH_3O$. In $H+O_2=O+OH$, the main chain branching reaction, more *O* and *OH* radicals are produced. The major pathway for NH_2 and *O* radical consumption is $NH_2+O=HNO+H$, where active radicals can be reduced. Additionally, most of the sensitivity coefficients decline (Fig. 18-b).

It can be understood from Fig. 17-b that by the increase of initial temperature from 300 to 473, an increase in *NO* formation is seen due to two significant factors. First, a higher temperature leads to a higher amount of radical's pool which plays a crucial role in producing *NO*. Second, increasing the initial temperature causes a rise in the flame temperature. It is attributed to increasing thermal *NO* formation.

The amount of *CO* increases by the increment of initial temperature from 300 to 473, while the amount of CO_2 decreases. Preheating the mixture provides parts of the required activation energy and helps generate a high radical pool level. Consequently, a good condition is provided for the reaction between CO_2 and CH_4, which causes increasing *CO* and *OH* radicals.

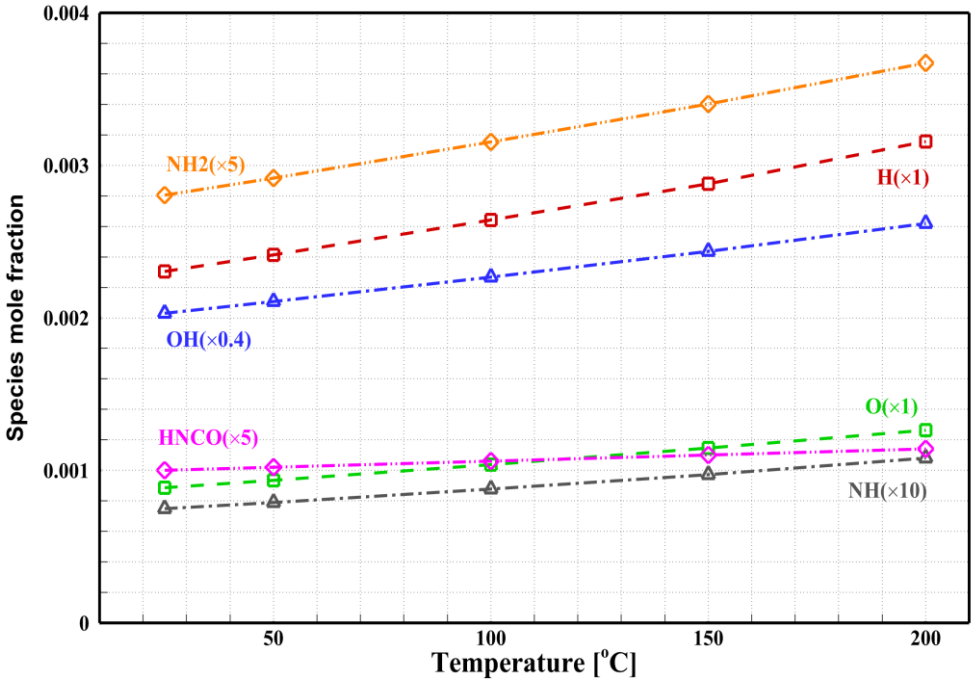

a

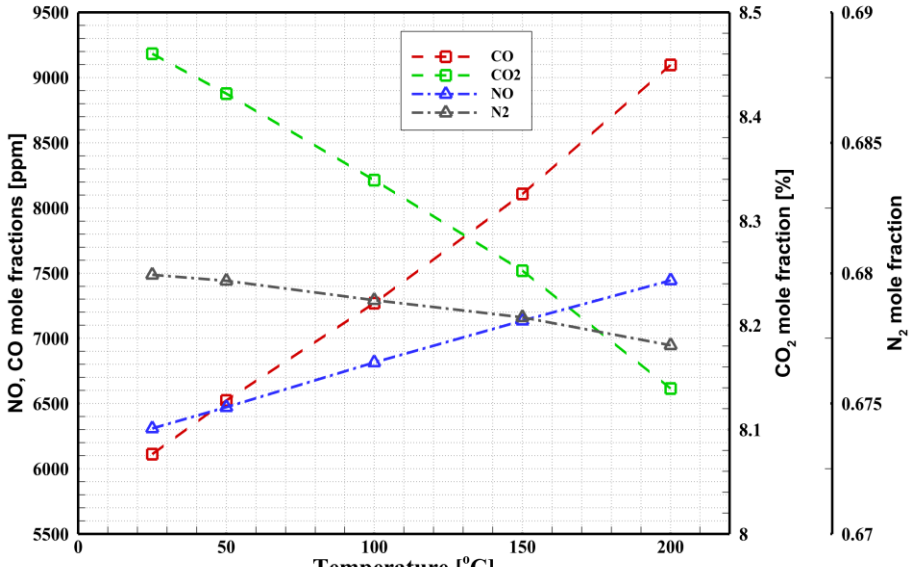

Fig. 17. Measured and Simulated radicals and emissions for different temperatures at α=0.4 ,β=0.7,P=1 bar and φ=1

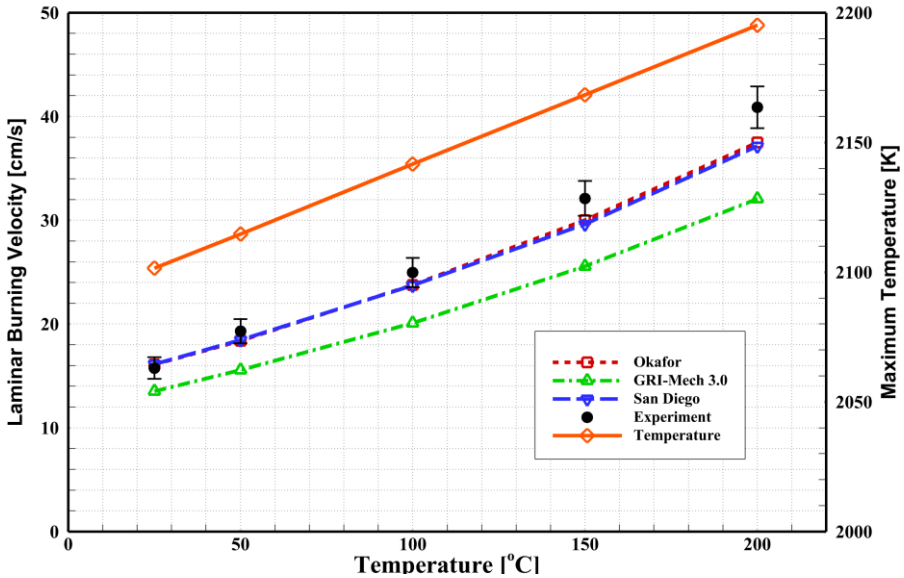

a

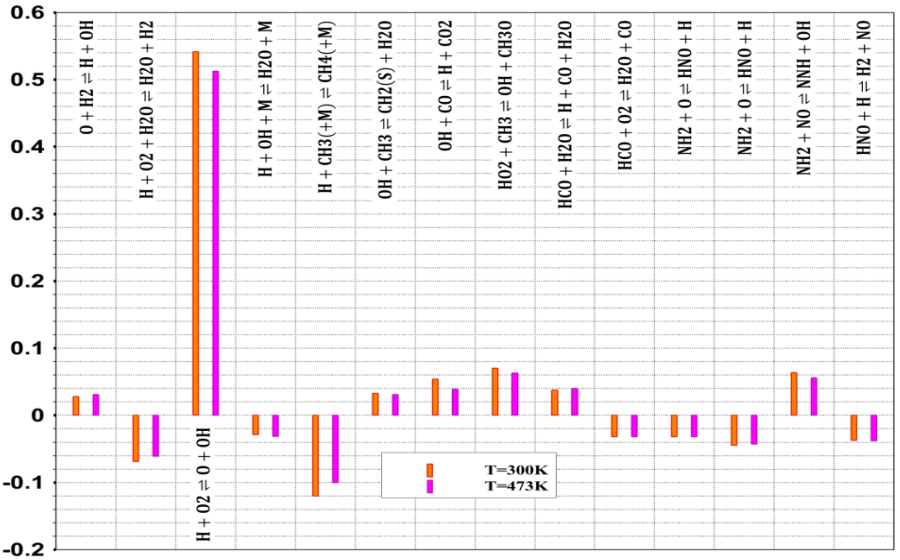

b

Fig. 18. measured and simulated flame speed and maximum flame temperature for different temperatures at α=0.4 ,β=0.7,P=1 bar and φ=1

Table 7. Comparison of experimental and numerical results under elevated temperature

T (K)	Exp.	Num. (Okafor)	GRI-Mech 3.0	San Diego
300	15.7	16	13.5	16.1
323	19.3	18.3	15.5	18.4
373	24.9	23.7	20	23.7
423	32.1	30	25.5	29.6
473	40.8	37.5	32	37.1

The preheating approach increases the kinetic energy (the higher number of molecular collisions and sufficient intermolecular energy for reaction), which increases the efficiency of the process. Therefore, it is expected that preheating results in a temperature increase Fig. 18-a.

5- Conclusion

Landfill gas is a biogas generated from organic waste and biomass which can have different compositions depending on production methods and sources. The accurate determination of combustion characteristics is crucial for its industrial use. To that end, this study investigates the fundamental combustion characteristics of Ammonia/LFG/Air, including variations in pressure and fuel composition. Flame characteristics like laminar burning velocity, and adiabatic temperature, as well as their interactions, were examined both experimentally and numerically. This data can assist in designing burners and chambers.

Increasing ammonia to landfill gas results in the flame turning more orange.

Given the chemistry of ammonia and methane, there has been no notable direct interaction observed between these fuels. Instead, they engage in competition for *O*/*H* radicals, crucial for both chain-branching and termination processes.

Increasing pressure results in a lower radical pool level. It reduces laminar burning velocity.

Increasing pressure increases adiabatic flame temperature due to alternation in the equilibrium point.

Concerning Le chatleliers principle, increasing pressure causes decreasing the mole number of radicals. Thus, pressure variation has an inverse effect on *NO* formation.

In rich conditions, there is a lot of chance of the conversion of NH_i to CH_2NH, which leads to more *HCN*. Thus, reactions move toward less *NO* by consuming NH_2 molecules.

Regarding the high reactivity of O_2, hydrocarbons react with this readily, which results in high *NO* formation.

The high CH_4 content in landfills provides a more substantial chemical effect, which increases the production of CH_2NH molecules.

The mixture's LBV is pulled down by the rising concentration of ammonia in the fuel mixture. Maximum flame temperature is decreased by increasing NH_3 concentration in the mix.

Increasing the initial temperature increases the radicals' pool level by weakening the bonds.

Two major factors of the high amount of *NO* formation in higher temperatures are a higher amount of radical pool level and maximum flame temperature.

Increasing the concentration of ammonia in the fuel mixture (up to $\alpha = 0.4$) first increases *NO* emission, then decreases it after ($0.4 < \alpha < 1$).

Nomenclature

A	Flame front's surface area
CDI	capacitor discharge ignition
C_p	Specific heat
D	Thermal diffusivity
Fps	Frame per seconds
k	Thermal conductivity
LBV	Laminar burning velocity
LFG	Landfill gas
P_i	Initial pressure
P_u	Pressure of unburned gas
R	radius
R_f	Flame front radius
S_l	Flame speed
S_b	Stretched flame propagation speed
S_b^0	Unstretched laminar flame speed
S_u	Stretched laminar flame speed
t	time
T_i	Initial temperature
Tot	Total
T_u	Temperature of unburned gas
u_c	Instrument error

u_i First order uncertainty

u_N Uncertainty

Greek symbols

α $\alpha = [NH_3]/[Tot]$

αT Temperature coefficient reflecting the temperature dependence

β $\beta = [CH_4]/[LFG]$

x_{NH_3} Ammonia mole fraction

φ Equivalence ratio

ρ Density (kg/m^3)

σ Expansion ratio of the gas

ρ_b density of the burned gas

ρ_u density of the unburned gas

κ Spherical flame's stretch rate

λ Wavelength of the laser beam (m)

Subscripts

i Mixture component comprising landfill fuel and air

u Unburned

References

[1] A. Valera-Medina, H. Xiao, M. Owen-Jones, W.I. David, P. Bowen. Ammonia for power, Progress in Energy and Combustion Science, 69 (2018) 63-102.

[2] H. Kobayashi, A. Hayakawa, K.K.A. Somarathne, E.C. Okafor. Science and technology of ammonia combustion, Proceedings of the Combustion Institute , 37(1) (2019) 109-133.

[3] M.P.G. Maab, S. Bathaei, M. Kim, J.A. Esfahani, K.C. Kim. Effect of air humidity on premixed combustion of ammonia/air under engine relevant conditions: numerical investigation, Journal of Thermal Analysis and Calorimetry, 148 (2023) 8347–8364.

[4] A.Hayakawa, T. Goto, R. Mimoto, Y. Arakawa, T. Kudo, H. Kobayashi. Laminar burning velocity and Markstein length of ammonia/air premixed flames at various pressures, Fuel, 159 (2015) 98-106.

[5] B. Mei, X. Zhang, S. Ma, M. Cui, H. Guo, Cao Z, Y. Li. Experimental and kinetic modeling investigation on the laminar flame propagation of ammonia under oxygen enrichment and elevated pressure conditions, Combust and Flame, 210 (2019) 236-246.

[6] X. Han, Z. Wang, M. Costa, Z. Sun, Y. He, K. Cen. Experimental and kinetic modeling study of laminar burning velocities of NH3/air, NH3/H2/air, NH3/CO/air and NH3/CH4/air premixed flames, Combust and Flame, 206 (2019) 214-226.

[7] E.C. Okafor, Y. Naito, S. Colson, A. Ichikawa, T. Kudo, A. Hayakawa, H. Kobayashi. Experimental and numerical study of the laminar burning velocity of CH4–NH3–air premixed flames, Combustion and Flame, 187 (2018) 185-198.

[8] E.C. Okafor, Y. Naito, S. Colson, A. Ichikawa, T. Kudo, A. Hayakawa, H. Kobayashi. Measurement and modelling of the laminar burning velocity of methane-ammonia-air flames at high pressures using a reduced reaction mechanism, Combustion and Flame, 204 (2019) 162-175.

[9] J. Zhang, D. Chen, S. Lai, J. Li, H. Huang, N. Kobayashi. Numerical simulation and spray model development of liquid ammonia injection under diesel-engine conditions, Energy, (2024) 130833.

[10] A.V. Mohod, M.V. Bagal. Technological developments in the energy generation from municipal solid waste (landfill gas capture, combustion, pyrolysis and gasification). 360-Degree Waste Management, 1 (2023) 139-157.

[11] C.A. Cardona, A.A. Amell. Laminar burning velocity and interchangeability analysis of biogas/C3H8/H2 with normal and oxygen-enriched air, International Journal of Hydrogen Energy, 38(19) (2013) 7994-8001.

[12] S. Elhawary, A. Saat, M.A. Wahid, M.Z.M. Zain. Effect of nitrous oxide on laminar burning velocity, hydrodynamic, and diffusive–thermal instability of biogas combustion, Journal of Thermal Analysis and Calorimetry, 148(8) (2023) 3073-3088.

[13] J. Beeckmann, L. Cai, H. Pitsch. Experimental investigation of the laminar burning velocities of methanol, ethanol, n-propanol, and n-butanol at high pressure, Fuel, 117 (2014) 340-350.

[14] A.Taqizadeh, O. Jahanian, S.I.P. Kani. Effects of equivalence and fuel ratios on combustion characteristics of an RCCI engine fueled with methane/n-heptane blend, Journal of Thermal Analysis and Calorimetry, 139 (20200 2541-2551.

[15] Z. Al-Hamamre, J. Yamin. The effect of hydrogen addition on premixed laminar acetylene–hydrogen–air and ethanol–hydrogen–air flames, International Journal of Hydrogen Energy, 38(18) (2013) 7499-7509.

[16] Y. He, Z. Wang, L. Yang, R. Whiddon, Z. Li, J. Zhou, K. Cen. Investigation of laminar flame speeds of typical syngas using laser based Bunsen method and kinetic simulation, Fuel, 95 (2012) 206-213.

[17] M. Kiani, E. Houshfar, M. Ashjaee. Experimental investigations on the flame structure and temperature field of landfill gas in impinging slot burners, Energy, 170 (2019) 507-520.

[18] L. Wang, Z. Liu, S. Chen, C. Zheng, J. Li. Physical and chemical effects of CO2 and H2O additives on counterflow diffusion flame burning methane, Energy & Fuels, 27(12) (2013) 7602-7611.

[19] E. Hu, X. Jiang, Z. Huang, N. Iida. Numerical study on the effects of diluents on the laminar burning velocity of methane–air mixtures, Energy & Fuels, 26(7) (2012)

4242-4252.

[20] N. Hinton, R. Stone. Laminar burning velocity measurements of methane and carbon dioxide mixtures (biogas) over wide ranging temperatures and pressures, Fuel, 116 (2014) 743-750.

[21] M.H. Askari, M. Ashjaee. Experimental measurement of laminar burning velocity and flammability limits of landfill gas at atmospheric and elevated pressures, Energy & Fuels, 31(3) (2017) 3196-3205.

[22] M. Kiani, E. Houshfar, M. Ashjaee. An experimental and numerical study on the combustion and flame characteristics of hydrogen in intersecting slot burners, International Journal of Hydrogen Energy, 43(5) (2018) 3034-3049.

[23] W. Hauf, U. Grigull. Advances in heat transfer. Advances in heat transfer, Academic, New York. 1970;6:133-136.

[24] R.D. Flack. Mach-Zehnder interferometer errors resulting from test section misalignment, Applied Optics, 17(7) (1978) 985-987.

[25] ANSYS Chemkin-Pro® Release 17.0 (Chemkin-Pro 15151) ANSYS, . 2016-01-11.

[26] M. Kohansal, M. Kiani, S. Masoumi, S. Nourinejad, M. Ashjaee, E. Houshfar. Experimental and numerical investigation of NH3/CH4 mixture combustion properties under elevated initial pressure and temperature, Energy & Fuels, 37(14) (2023) 10681-10696.

[27] R. Bardolf, F. Winter. Comparison of chemical kinetic mechanisms for combustion simulation of treated biogas, The Holistic Approach to Environment, 4(2) (2014) 65-69.

[28] D.R. Dowdy, D.B. Smith, S.C. Taylor, A. Williams, editors. The use of expanding spherical flames to determine burning velocities and stretch effects in hydrogen/air mixtures. Symposium (International) on Combustion, 1991: Elsevier.

[29] G. Sivashinsky. On a distorted flame front as a hydrodynamic discontinuity, Acta Astronaut, 3(11-12) (1976) 889-918.

[30] M. Matalon, B.J. Matkowsky. Flames as gasdynamic discontinuities, Journal of Fluid Mechanics, 124 (1982) 239-259.

[31] P. Clavin. Dynamic behavior of premixed flame fronts in laminar and turbulent flows, Progress in Energy and Combustion Science, 11(1) (1985) 1-59.

[32] A.P. Kelley, C.K. Law. Nonlinear effects in the extraction of laminar flame speeds from expanding spherical flames, Combust and Flame, 156(9) (2009) 1844-1851.

[33] H. Kobayashi, T. Tamura, K. Maruta, T. Niioka, F.A. Williams, editors. Burning velocity of turbulent premixed flames in a high-pressure environment. Symposium (International) on Combustion; 1996: Elsevier.

[34] A.A. Konnov, A. Mohammad, V.R. Kishore, N.I. Kim, C. Prathap, S. Kumar. A comprehensive review of measurements and data analysis of laminar burning velocities for various fuel+ air mixtures, Progress in Energy and Combustion Science, 68 (2018) 197-267.

[35] Z. Chen. On the accuracy of laminar flame speeds measured from outwardly propagating spherical flames: Methane/air at normal temperature and pressure, Combustion and Flame. 162(6) (2015) 2442-2453.

[36] H. Yu, W. Han, J. Santner, X. Gou, C.H. Sohn, Y. Ju, Z. Chen. Radiation-induced uncertainty in laminar flame speed measured from propagating spherical flames, Combustion and Flame, 161(11) (2014) 2815-2824.

[37] M.P. Burke, Z. Chen, Y. Ju, F.L. Dryer. Effect of cylindrical confinement on the determination of laminar flame speeds using outwardly propagating flames, Combustion and Flame, 156(4) (2009) 771-779.

[38] P.D. Ronney, H.Y. Wachman. Effect of gravity on laminar premixed gas combustion I: Flammability limits and burning velocities, Combustion and Flame, 62(2) (1985) 107-119.

[39] B. Mei, S. Ma, Y. Zhang, X. Zhang, W. Li, Y. Li. Exploration on laminar flame propagation of ammonia and syngas mixtures up to 10 atm, Combust and Flame, 220 (2020) 368-377.

[40] T. Mendiara, P. Glarborg. Ammonia chemistry in oxy-fuel combustion of methane, Combustion and Flame, 156(10) (2009) 1937-1949.

[41] H. Mikulčić, J. Baleta, X. Wang, J. Wang, F. Qi, F. Wang. Numerical simulation of ammonia/methane/air combustion using reduced chemical kinetics models, International Journal of Hydrogen Energy, 2021.

[42] H. Xiao, A. Valera-Medina, R. Marsh, P.J. Bowen. Numerical study assessing various ammonia/methane reaction models for use under gas turbine conditions, Fuel, 196 (2017) 344-3451.

[43] P. Sabia, G. Sorrentino, A. Chinnici, A. Cavaliere, R. Ragucci. Dynamic behaviors in methane MILD and oxy-fuel combustion. Chemical effect of CO2, Energy Fuels, 29(3) (2015) 1978-1986.

[44] D. Yossefi, S. Ashcroft, J. Hacohen, M. Belmont, I. Thorpe. Combustion of methane and ethane with CO2 replacing N2 as a diluent. Modelling of combined effects of detailed chemical kinetics and thermal properties on the early stages of combustion, Fuel. 74(7) (1995) 1061-1071.

[45] I.Iliuta, R. Tahoces, G.S. Patience, S. Rifflart, F. Luck. Chemical-looping combustion process: Kinetics and mathematical modeling, AICHE Journal 56(4) (2010) 1063-1079.

[46] C.E. Loo, N, Tame, G.C. Penny. Combustion Physics, ISIJ International (2012) 52(6):967-76.

[47] E.L. Cussler. Diffusion: Mass Transfer in Fluid Systems: Cambridge University Press; 2009.

[48] D.J. Bellamy, P.H. Clarke. Application of the Second Law of Thermodynamics and Le Chatelier's Principle to the Developing Ecosystem, Nature, 218(5147)

(1968)1180-1180.

[49] P. Sabia, G. Sorrentino, P. Bozza, G. Ceriello, R. Ragucci, M. De Joannon. Fuel and thermal load flexibility of a MILD burner, Proceedings of the Combustion Institute, 37(4) (2019) 4547-4554.

[50] P. Glarborg, L.L. Bentzen. Chemical effects of a high CO2 concentration in oxy-fuel combustion of methane, Energy and Fuels. 22(1) (2008) 291-296.

[51] L. Andrussow. Über die schnell verlaufenden katalytischen Prozesse in strömenden Gasen und die Ammoniak-Oxydation (V). Berichte der deutschen chemischen Gesellschaft (A and B Series), 60(8)) (1927) 2005-2018.

[52] C. Lhuillier, P. Brequigny, N. Lamoureux, F. Contino, C. Mounaïm-Rousselle. Experimental investigation on laminar burning velocities of ammonia/hydrogen/air mixtures at elevated temperatures, Fuel, 263 (2020) 116653.

[53] Ø. Skreiberg, P. Kilpinen, P. Glarborg. Ammonia chemistry below 1400 K under fuel-rich conditions in a flow reactor, Combustion and Flame, 136(4) (2004) 501-518.

HOW TO CITE THIS ARTICLE

M. Kiani, A. A. Abbasian Arani, M. Ashjaee, E. Houshfar, Exploring Flame Characteristics of CH4/CO2/Ammonia/Air Mixtures under Elevated Conditions: An Interferometry-Based Investigation, AUT J. Mech Eng., 7(4) (2023) 389-418.

DOI: 10.22060/ajme.2024.23011.6092